Cerebral tomoelastography based on multifrequency MR elastography in two and three dimensions

Helge Herthum, Stefan Hetzer, Bernhard Kreft, Heiko Tzschätzsch, Mehrgan Shahryari, Tom Meyer, Steffen Görner, Hennes Neubauer, Jing Guo, Jürgen Braun, Ingolf Sack

Cerebral tomoelastography based on multifrequency MR elastography in two and three dimensions.

Helge Herthum[1,2,3], Stefan Hetzer[2,3], Bernhard Kreft[4], Heiko Tzschätzsch[4], Mehrgan Shahryari[4], Tom Meyer[4], Steffen Görner[4], Hennes Neubauer[4], Jing Guo[4], Jürgen Braun[1], Ingolf Sack[4*]

[1]Institute of Medical Informatics, Charité – Universitätsmedizin Berlin, Corporate Member of Freie Universität Berlin, Humboldt-Universität zu Berlin, and Berlin Institute of Health, 10117, Berlin, Germany
[2]Berlin Center for Advanced Neuroimaging, Charité – Universitätsmedizin Berlin, Corporate Member of Freie Universität Berlin, Humboldt-Universität zu Berlin, and Berlin Institute of Health, 10117, Berlin, Germany
[3]Bernstein Center for Computational Neuroscience, Charité – Universitätsmedizin Berlin, Corporate Member of Freie Universität Berlin, Humboldt-Universität zu Berlin, and Berlin Institute of Health, 10117, Berlin, Germany
[4]Department of Radiology, Charité – Universitätsmedizin Berlin, Corporate Member of Freie Universität Berlin, Humboldt-Universität zu Berlin, and Berlin Institute of Health, 10117, Berlin, Germany

***Corresponding author:**

Ingolf Sack, PhD
Department of Radiology
Charité – Universitätsmedizin Berlin
Charitéplatz 1
10117 Berlin, Germany
Tel +49 30 450 539058
Ingolf.sack@charite.de

Abstract

Purpose: Magnetic resonance elastography (MRE) generates quantitative maps of the mechanical properties of biological soft tissues. However, published values obtained by brain MRE vary largely and lack detail resolution, due to either true biological effects or technical challenges. We here introduce cerebral tomoelastography in two and three dimensions for improved data consistency and detail resolution while considering aging, brain parenchymal fraction (BPF), systolic blood pressure, and body-mass-index.

Methods: Multifrequency MRE with 2D- and 3D-tomoelastography postprocessing was applied to the brains of 31 volunteers (age range:22-61years) for analyzing the coefficient of variation (CV) and effects of biological factors. Eleven volunteers were rescanned after one day and one year to determine intraclass correlation coefficient (ICC) and identify possible long-term changes.

Results: White matter shear-wave-speed (SWS) was slightly higher in 2D-MRE (1.28±0.02m/s) than 3D-MRE (1.22±0.05m/s,$p<0.0001$), with less variation after one day in 2D (0.33±0.32%) than in 3D (0.96±0.66%,$p=0.004$), which was also reflected in a slightly lower CV and higher ICC in 2D (1.84%, 0.97 [0.88-0.99]) than in 3D (3.89%, 0.95 [0.76-0.99]). Remarkably, 3D-MRE was sensitive to a decrease in white matter SWS within only one year, whereas no change in white matter volume was observed during this follow-up period. Across volunteers, stiffness correlated with age and BPF, but not with blood pressure and body-mass-index.

Conclusions: Cerebral tomoelastography provides high-resolution viscoelasticity maps with excellent consistency. Brain MRE in 2D shows less variation across volunteers in shorter scan times than 3D-MRE, while 3D-MRE appears to be more sensitive to subtle biological effects such as aging.

Keywords: multifrequency MRE; viscoelasticity; brain; reproducibility

Introduction

Magnetic resonance elastography (MRE) is an emerging imaging modality which allows in vivo assessment of soft tissue mechanics.[1-3] MRE generates quantitative maps of the mechanical properties of biological tissues by stimulating, encoding, and numerically analyzing shear waves. In neuronal applications, MRE has been proven sensitive to disease and physiological effects both for 2D and 3D wave inversion.[3-6] Prominent examples include brain softening during aging[7-9] and Alzheimer's disease[10-12], multiple sclerosis[13, 14], Parkinson's disease[15, 16], and normal pressure hydrocephalus[17, 18]. Conversely, brain stiffening has been reported as a result of jugular compression[19], Valsalva maneuver[20], hypercapnia[21], perfusion pressure[22], idiopathic intracranial hypertension[23], and functional activation[24, 25].

Specifically, aging has been reported to be associated with up to 0.8% brain softening per year in adults.[7] Alzheimer's disease and multiple sclerosis contribute 8%[12, 26] to 20%[13, 14, 27] lower brain stiffness while changes in blood perfusion have smaller effects of only 2% to 5%[21, 22]. Focal changes such as tumors are delineable by MRE when lesions markedly alter brain stiffness on the order of 100% and, thus, generate robust contrast in viscoelasticity maps[28, 29].

However, possible changes in smaller multiple sclerosis lesions might be masked by blurry or noisy MRE maps, which cannot display interfaces between small anatomical subregions.[30] For example, deep gray matter (DGM) regions such as the putamen, caudate nucleus, or globus pallidum are still difficult to detect using viscoelasticity maps, which hinders diagnostic applications of brain MRE in those regions.[31-33] Moreover, in disseminated pathologies that affect larger brain regions, MRE is hampered by a relatively wide inter-subject variability of stiffness values. For example, differences in brain stiffness of 13% to 20% have been reported between healthy individuals of similar age [12] using the same MRE method[31, 34, 35].[6]. It is still unclear whether this variability is due to methodological differences, geometrical reasons such as individual brain morphology, physiological influences including blood pressure and body mass index (BMI), or, if intrinsic structural differences among individuals result in distinct brain stiffness values.

Taken together, we identified two main challenges for the clinical application of state-of-the-art cerebral MRE: first, limited resolution of detail and, second, large inter-subject variability. And it remains to be determined if these challenges reflect technical limitations or biological margins of variability of brain viscoelasticity.

Regarding technical challenges, it has been discussed that 3D MRE provides more consistent measurements than 2D MRE because wave patterns in the reverberant skull are rather complex in space and encounter wave guide effects which might disturb planar projections.[36, 37] On the other hand, 2D inversion algorithms are less prone to interslice artifacts and do not require full brain coverage, which expedites image acquisitions of thinner slabs through the tissue of interest.[38, 39] To tackle the longstanding question of whether 2D or 3D MRE is preferable for intracranial applications we developed a brain processing pipeline which exploits wavenumber (*k*)-based multifrequency dual elasto-visco (*k*-MDEV) inversion in two variants, once with shear wave separation in 3D using the curl operator and once with 2D bandpass filtering. *k*-MDEV supports multifrequency inversion as included in the tomoelastography pipeline that has been used in many multifrequency MRE applications in abdominal and pelvic organs[40-42]. We chose this tomoelastography approach because *k*-MDEV because it invokes first-order gradients instead of second-order Laplacian operators, making it more robust against noise than direct inversion approaches. Consequently, we expect less noise-related artifact than with previous methods and hope to thus achieve better detail resolution and data consistency.

Here, we simply assess detail resolution based on visual comparison with the naked eye of anatomical detail depicted in standard anatomical MRI and MRE. For example, DGM subregions vary in their relaxation times, providing imaging contrast in conventional MRI. Reproducing regional image contrasts of anatomical structures based on shear wave speed would fundamentally change our perception of brain MRE maps as a source of tomographic information beyond regional mean values.

Consistency is assessed in our study by the cross-sectional and longitudinal variation of MRE values across larger anatomical areas (global brain tissue [GBT], cortical gray matter [CGM], white matter [WM], and DGM) as well as the reproducibility of values.

Reproducibility is addressed by repeated measurement after a day while longitudinal variation due to possible aging effects is studied by repeated examinations after one year.

Regarding the sensitivity of brain MRE to biological effects, we study possible biological influences (cross-sectional age, longitudinal aging, peripheral blood pressure, BMI) and geometrical influences (brain parenchyma fraction, BPF) including wave amplitudes on the measured values by correlation analysis.

Collectively, we aim to

(i) provide reference values for cerebral tomoelastography of the brain,
(ii) demonstrate high-resolution viscoelasticity mapping of anatomical detail,
(iii) assess the short-term and long-term consistency of the method based on one-day and one-year follow-up examinations, and
(iv) discuss pros and cons of 2D and 3D wave inversion in MRE of the brain.

Methods

Volunteers

We included 31 healthy volunteers (12 women; mean age ± standard deviation [SD]: 34 ± 11 years, age range: 22 to 61 years) in this study. A subgroup of eleven volunteers (3 women; mean age ± SD: 32 ± 9 years, age range: 22 to 46 years) were examined two additional times, one day and one year after the baseline examination. All volunteers underwent both standard anatomical MRI and multifrequency MRE.

The study was approved by the ethics committee of Charité – Universitätsmedizin Berlin in accordance with the Ethical Principles for Medical Research Involving Human Subjects of the World Medical Association Declaration of Helsinki. All volunteers gave informed written consent prior to the imaging examinations.

Standard anatomical MRI

All experiments were performed in a 3-Tesla MRI scanner (Siemens Lumina, Erlangen, Germany) equipped with a 32-channel head coil. Each volunteer's head was placed exactly in the same position on the vibration bed with precise connection to the driver

during all follow-up examinations. All slice blocks were automatically positioned at the center of the brain using the scanner's auto align function based on the localizer scan. T1-weighted, high-resolution, whole-brain images were acquired using a magnetization-prepared rapid acquisition of gradient echo sequence (MPRAGE; echo time: 2.27 ms, repetition time: 2300 ms, inversion time: 900 ms, flip angle of 8°, isotropic voxel size of 1 mm^3). WM volume and the brain parenchymal fraction (BPF), which is the ratio of intracranial brain parenchymal volume (GM plus WM) to total intracranial volume (GM plus WM plus cerebrospinal fluid), were calculated from MPRAGE images using *SPM-segment* in SPM12[43].

MRE experimental setup

Multifrequency MRE was performed using a single-shot, spin-echo, echo-planar imaging (EPI) sequence.[35] Eight phase offsets equally spaced over a vibration period were recorded for 40 axial slices for each harmonic vibration induced at 20, 25, 30, and 35 Hz using pressurized air drivers as described elsewhere[44]. Three displacement components in orthogonal directions were encoded using a flow-compensated, motion-encoding gradient with an amplitude of 34 mT/m and a duration of 28 ms. Encoding efficiencies were 12.4, 8.9, 7.1, and 6.2 µm/rad for 20, 25, 30, and 35 Hz, respectively. Further imaging parameters were: field of view 202 x 202 mm^2, voxel size 1.6 × 1.6 × 2 mm^3, echo time 70 ms, repetition time 4700 ms. GRAPPA parallel acquisition[45] with an acceleration factor of 2 was used. Moreover, two images with inverted phase-encoding direction were recorded for distortion correction. Total acquisition time for a full set of 3D multifrequency MRE data was approximately 8 min.

Motion and distortion correction

Complex MRE images were corrected in a slice-wise fashion (2D) for stochastic head motion and field distortions using *SPM-realign* and *Hysco2* (based on field maps with inverted readout direction), respectively, in SPM12. Mean MRE magnitude images were calculated by averaging over the frequencies, encoding directions, and time steps and normalized to the Montreal Neurological Institute (MNI) space based on the ICBM152

template[46] using SPM12. Generated transformation matrices were used for normalization of viscoelastic parameter maps.

MRE data analysis

Shear wave speed (SWS) and penetration rate (PR) maps[47] were reconstructed using wavenumber-based (*k*-)MDEV inversion[38] with recently introduced, brain-adapted pre-processing[30, 48, 49]. SWS is related to tissue stiffness and will be termed as such where appropriate. PR reflects inverse viscosity, i.e., the deeper the shear waves penetrate into the tissue the less viscous the tissue behaves. Reconstructions were performed 2D (slice-wise) and fully 3D using a newly developed processing pipeline. For 2D data processing, wave images were decomposed in eight propagation directions. Smoothing and suppression of compression waves were done using a bandpass Butterworth filter of third order with a highpass threshold of 15 1/m and lowpass threshold of 250 1/m. The 2D pipeline is publicly available on https://bioqic-apps.charite.de/.[50] For 3D data processing, slice phase offsets and interphase discontinuities between slices were removed after temporal Fourier transform according to Barnhill *et al*.[51]. The corrected images were smoothed with a lowpass Butterworth filter of first order and threshold of 200 1/m. Single-direction shear wave fields were computed using the 3D curl operator with 3-pixel symmetric derivative kernels followed by spatial filtering into 20 directions equally distributed over a 3D sphere. SWS and PR maps were reconstructed based on 3D phase gradients. Due to edge slice artifacts of the 3D inversion, the four outermost slices in each direction were removed, leaving 32 slices for further analysis. The same number of slices was discarded from our 2D analysis to ensure comparability of values obtained in the same volumes.

SWS and PR maps were normalized to the MNI space using the mean MRE magnitude images to generate averaged parameter maps and tissue probability maps[43]. Probability maps for WM, CGM, and DGM were thresholded at 0.5 to generate segmentation masks. Probabilities for cerebrospinal fluid were thresholded at 0.1 and excluded from other masks to avoid tissue-fluid boundary artifacts. Spatially averaged values were determined in the following regions: GBT, WM, CGM, and DGM as well as DGM subregions: nucleus accumbens (Ac), nucleus caudate (Ca), globus pallidus (Pal),

putamen (Pu), and thalamus (Th). The hippocampus and amygdala were not included since both regions were only covered partially due to their basal positions within the scan volume. In addition, average wave amplitudes were determined in the respective brain regions.

Dependence of 3D SWS values on number of slices

In eleven volunteers, we further analyzed how the number of slices for a fixed slice block thickness potentially affected SWS and PR values in 3D processing. Starting with 3D processing based on 39 slices, equivalent to 62.4 mm block thickness, we averaged SWS and PR within WM visible in the center slice for reference, and, subsequently, removed the two outermost slices from further 3D processing. The error (in %) relative to the central reference slice was averaged over all volunteers. Data were processed in MATLAB 2020a (Mathworks Inc. Natick, MN, USA).

Statistical analysis

Cross-sectional investigations provided inter-subject variability based on the coefficient of variation (CV) in all brain regions we analyzed. Correlations between reconstructed parameters (2D-SWS, 2D-PR, 3D-SWS, and 3D-PR) and region-specific wave amplitude, age, systolic peripheral blood pressure (BP), BMI, and BPF were analyzed in GBT using Pearson's correlation coefficient. P-values were corrected for four comparisons using the Holm-Bonferroni method. A multivariable linear regression model with age and BPF as independent variable was calculated for SWS and PR, respectively (e.g., SWS = intercept + beta1*BPF + beta2*age).

Differences between viscoelastic values reconstructed from 2D and 3D inversion and between different brain regions (WM vs CGM and WM vs DGM) were analyzed using a paired Student's t-test and a correlation analysis. P-values were corrected for multiple comparisons using the Holm-Bonferroni method.

Repeated measurements in eleven volunteers after one day provided reproducibility indices for 2D and 3D data processing based on mean relative absolute difference (RAD) and intraclass correlation coefficient (ICC) for GBT, WM, CGM, and DGM. RAD between

2D and 3D data processing was compared using a paired Student's t-test. ICC estimates and their 95% confident intervals were based on a single-rater, absolute-agreement, two-way, mixed-effects model.[52-54] One-year follow-up measurements were compared with earlier measurements in the same volunteer to test for a possible aging effect on values in the GBT, WM, CGM, and DGM. Therefore, we performed two separate paired Student's t-tests for each region. P-values were corrected for two comparisons using the Holm-Bonferroni method.

All statistical analysis was done in R version 4.0.2 (R-Foundation, Vienna, Austria). P-values below 0.05 were considered statistically significant.

Results

The analyzed MRE volumes covered 65% GBT, 77% WM, 53% CGM, and 84% DGM of the MNI volume, resulting in group-averaged volumes of 909 ± 44 cm^3, 544 ± 21 cm^3, 380 ± 22 cm^3, and 53 ± 5 cm^3, respectively. Mean BPF was 0.77 ± 0.04%.

Figure 1 shows three representative slices in MNI space of group-averaged SWS generated by 2D and 3D processing along with anatomical reference images from the MNI atlas. Masks for WM, CGM, and DGM, after the exclusion of cerebrospinal fluid, are demarcated by colored lines while red arrows indicate where 3D boundary artifacts propagated through the slices. Both approaches resulted in high-resolution SWS maps with details of anatomy which visually matched the anatomical reference images. Tissue boundaries were well defined and DGM regions could be visually differentiated from WM based on SWS. Fluid-filled spaces appeared larger in 3D SWS than 2D SWS maps, because the curl operator implied in 3D processing enhanced boundary effects by spatial derivatives [55], while noise in air was better suppressed by 3D than 2D processing. Mean WM SWS values were slightly higher for 2D (1.28 ± 0.02 m/s) than 3D processing (1.22 ± 0.05 m/s, $p < 0.0001$). Both reconstruction methods yielded higher SWS values for DGM (2D: 1.42 ± 0.09 m/s, 3D: 1.29 ± 0.09 m/s) and lower SWS values for CGM (2D: 1.21 ± 0.03 m/s, 3D: 1.09 ± 0.05 m/s) compared with WM ($p < 0.0001$ for each test). Group statistical plots for GBT, WM, CGM, and DGM in 2D and 3D are shown in Figure 2. A descriptive summary for all analyzed regions is given in Table 1, including region size and

CV. Inter-subject variations as quantified by CV were smaller in 2D than 3D processing. CV in GBT, WM, CGM, and DGM was 2.3%, 1.8%, 2.5%, and 6.1% in 2D MRE versus 4.1%, 3.9%, 4.7%, and 6.7% in 3D MRE, respectively (see also Figure 6 and Table 3). Figure 3 shows a correlation plot for 2D and 3D SWS values for GBT. The results for both approaches were highly correlated ($r = 0.75$, $p < 0.0001$). A corresponding analysis is provided for the viscosity-related PR parameter in the supplemental material. In short, 2D-PR was markedly higher than 3D-PR (e.g., for GBT: 0.83 ± 0.04 m/s vs. 0.56 ± 0.03). CVs were higher than for SWS and similar between 2D and 3D (e.g., for GBT: 5.4% for 2D and 4.4% for 3D).

Correlation analysis

SWS in GBT was negatively correlated with age (2D: $r = -0.54$, $p = 0.007$, 3D: GBT: $r = -0.45$, $p = 0.04$) and positively correlated with BPF (2D: $r = 0.72$, $p < 0.0001$, 3D: GBT: $r = 0.68$, $p = 0.0001$). The annual change in SWS of GBT was -0.0014 m/s in 2D (95%-CI: [-0.0022, -0.0006]) and -0.0019 m/s in 3D (95%-CI: [-0.0034, -0.0005]). Multivariable analysis for SWS in GBT showed a significant effect of BPF on SWS (beta1 = 0.49, standard error = 0.14, $p = 0.001$) while no significant effect of age was observed (beta2 = -0.00027, standard error = 0.0004, $p = 0.54$) given an intercept of 0.90 (standard error = 0.11).

2D SWS of DGM was correlated with wave amplitudes in DGM (mean ± SD: 10.8 ± 2.5 µm, range: 6.4 – 15.9 µm, $r = 0.45$, $p = 0.035$, slope: 0.015 m/s / µm) while no such correlation was observed in 3D. SWS was not correlated with BP or BMI. A correlation analysis of PR, presented in the supplemental material, showed that PR correlated most markedly with wave amplitude in 2D and 3D and only slightly with BPF in 3D.

Repeated SWS measurement

Figure 4 shows the reconstructed SWS maps in a representative slice from one volunteer examined at three time points: baseline, one day later, and after one year for both 2D and 3D processing. No differences between the three measurements were visually apparent. Remarkably, subtle differences between DGM subregions were already apparent based on individual SWS maps and were consistent with group mean values (Figure 1 and Table

1). For example, putamen (yellow arrow) appeared as the stiffest DGM region - in agreement with the results compiled in Table 1 and published values[22] - and was even distinguishable by eye from globus pallidus (red arrow) in the 3D SWS maps shown in the figure, again in agreement to group mean values (17% difference, $p < 0.0001$). Again, fluid-filled spaces were slightly enlarged by 3D data processing, however, with lower noise than visible in 2D SWS maps.

Group-averaged SWS values (2D and 3D for GBT, WM, CGM, and DGM) measured at three time points in eleven volunteers are presented in Figure 5. Inter-subject variability, assessed by CV, as well as reproducibility between baseline and retest one day later, assessed by ICC and mean RAD (within-subject variability), were derived from these results and are displayed in Figure 6. Tables 2 and 3 summarize the one-day test-retest and one-year follow-up results, respectively.

Figure 6 shows CV values for 2D and 3D data processing based on all volunteers and as an average of individual CVs from baseline, 1-day, and 1-year measurements for eleven volunteers. CV for the total group and subset group ($n = 31$ and $n = 11$) was similar. CV for 2D processing was markedly lower than for 3D processing with the lowest values measured in WM and highest values in DGM. As shown in Figure 6 and indicated by ICC ≥ 0.95, very good reproducibility was achieved for both pipelines. ICC 95% confidence intervals obtained in 2D were smaller than in 3D. Mean RAD between repeated measurements indicated better reproducibility for 2D than 3D processing ($p=0.004$ for WM). Specifically, mean RAD was lowest for 2D WM SWS (0.33 ± 0.32%) and increased for GBT (0.43 ± 0.33%), CGM (0.68 ± 0.46%), and DGM (1.31 ± 1.06%). 3D values for GBT, WM, CGM, and DGM were 1.16 ± 0.71%, 0.96 ± 0.66%, 1.47 ± 0.98%, and 1.34 ± 1.17%, respectively. A summary for CV, ICC and RAD is given in Table 2. The corresponding analysis for penetration rate, PR, presented as supplemental information, revealed similarly excellent reproducibility of viscosity-related PR for 2D and 3D reconstruction (e.g., ICC in GBT: 0.94 for 2D and 0.98 for 3D). However, the 3D reconstruction showed lower variability for PR than 2D (e.g., mean RAD in GBT: 0.84 ± 0.74% vs. 1.72 ± 1.22%).

Significant brain softening after one year was observed in GBT, WM, CGM, and DGM using 3D reconstruction. In WM, SWS changed between baseline and 1-year follow-up by -0.011 m/s (95%-CI: [-0.021, -0.001], p = 0.037) and between day one and 1-year follow-up by -0.021 (95%-CI: [-0.032, -0.010], p = 0.007). This longitudinal decrease in SWS, most likely attributable to aging, was about tenfold higher than obtained from our previously reported cross-sectional analysis in 31 brains. In contrast, no significant change in WM volume was observable after one year, whereas BPF was significantly reduced by 1.1 ± 1.0% (p = 0.019).

Dependence of 3D SWS values on number of slices

Figure 7 demonstrates how 3D SWS averaged within WM of the center slice is affected by the total number of input slices for a fixed block thickness. The mean relative error was obtained from eleven volunteers and computed by taking WM 3D SWS of the full 39-slice input data as a reference while subsequently reducing the number of slices by removing the outermost slice pair. For each computation, central-slice SWS was averaged within WM and normalized with reference SWS of the same region. It is apparent that reference SWS is increasingly underestimated (more than 10%) as the total slice number is successively reduced to less than nine slices, indicating the inaccuracy of 3D MRE in thinner slabs.

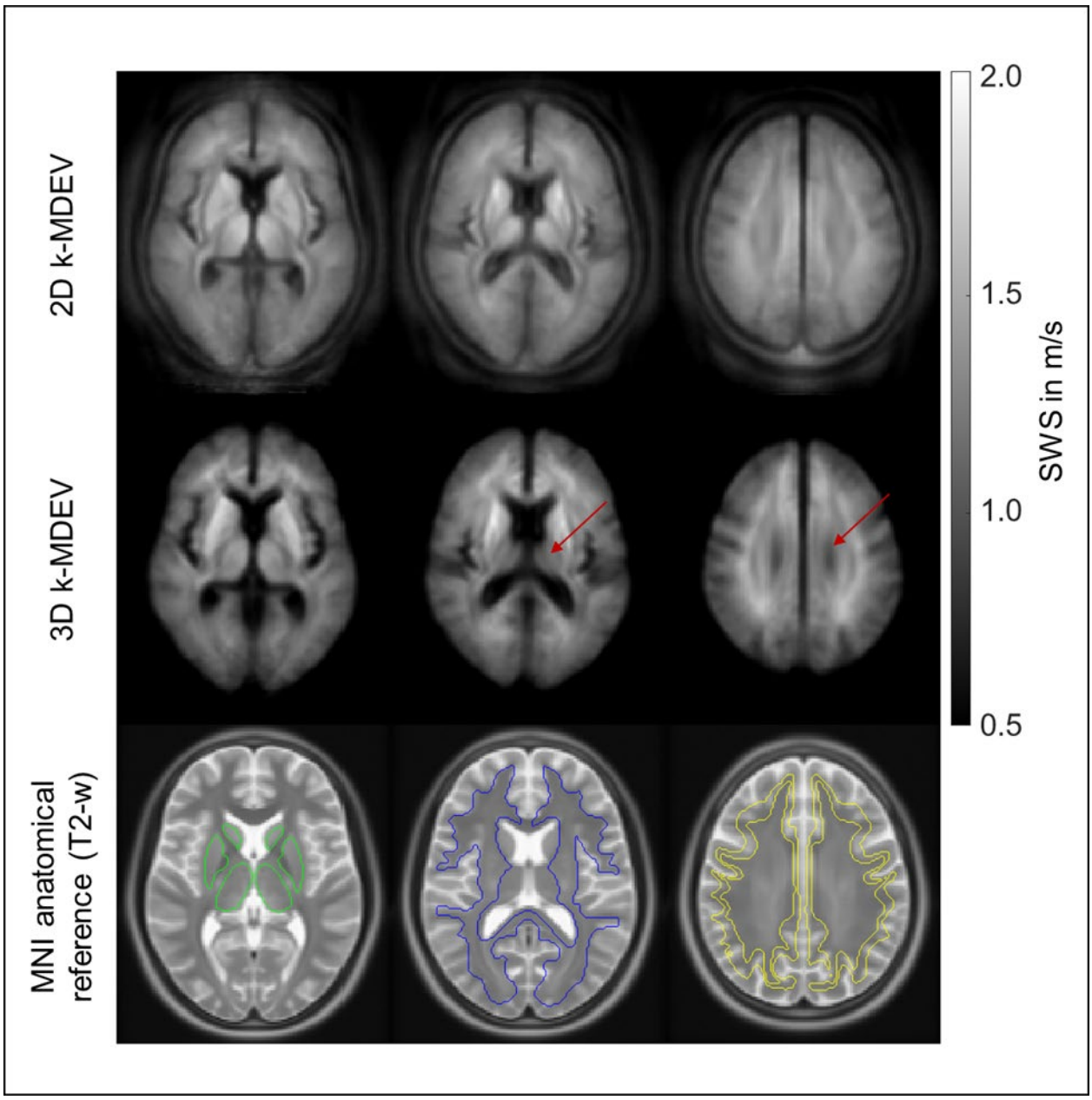

Figure 1: Averaged SWS maps from 2D and 3D *k*-MDEV inversions normalized to MNI space in three representative slices. Red arrow indicates where boundary artifacts from adjacent slices become visible in 3D reconstruction. Anatomical reference images (ICBM152 template) are shown superimposed with atlas regions for deep gray matter (green), white matter (blue), and cortical gray matter (yellow).

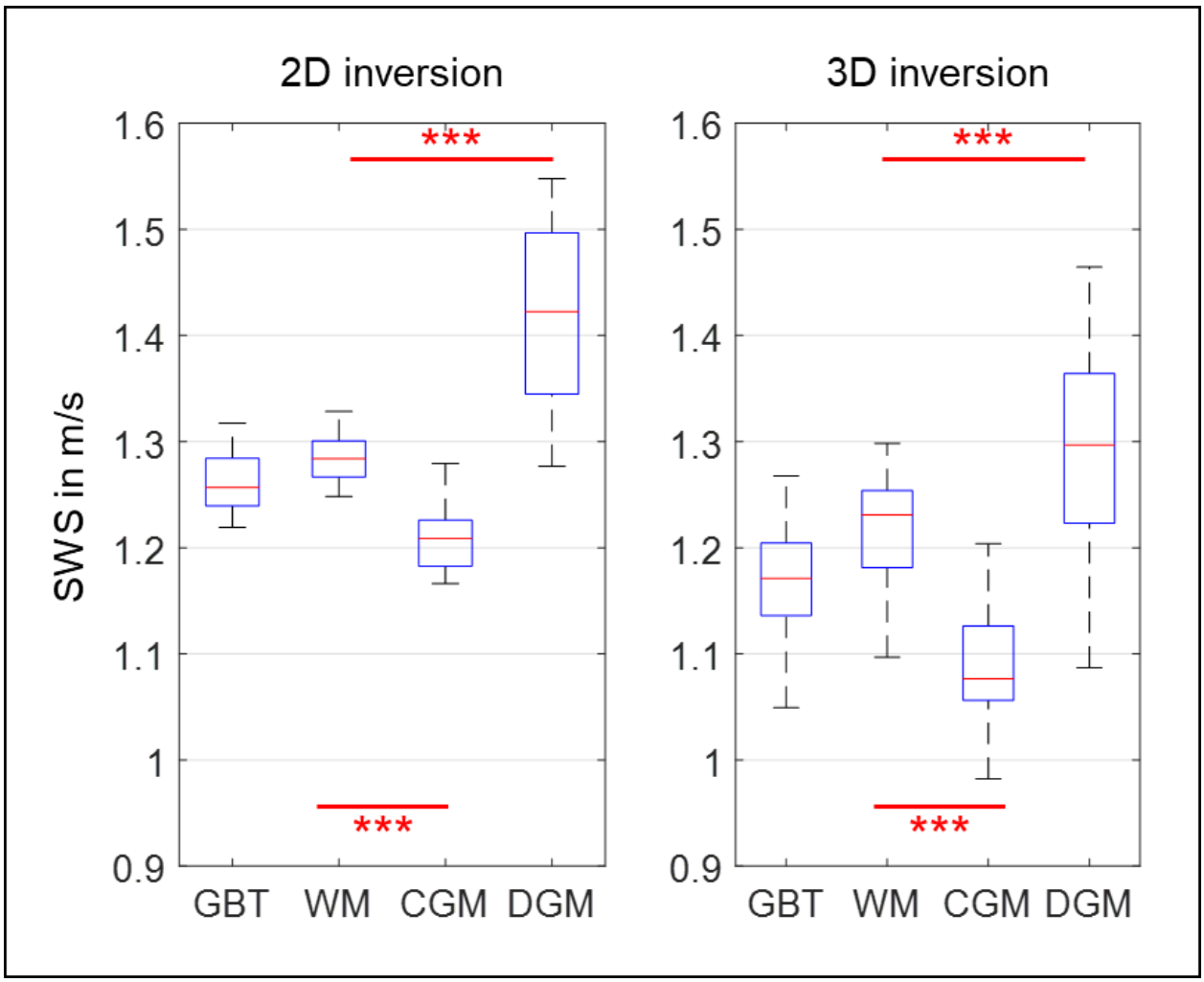

Figure 2: Group mean SWS values for 2D and 3D *k*-MDEV for global brain tissue (GBT), white matter (WM), cortical gray matter (CGM), and deep gray matter (DGM). Significance levels, indicated by asterisks, were determined from paired t-tests with Holm-Bonferroni correction between WM and CGM as well as WM and DGM.

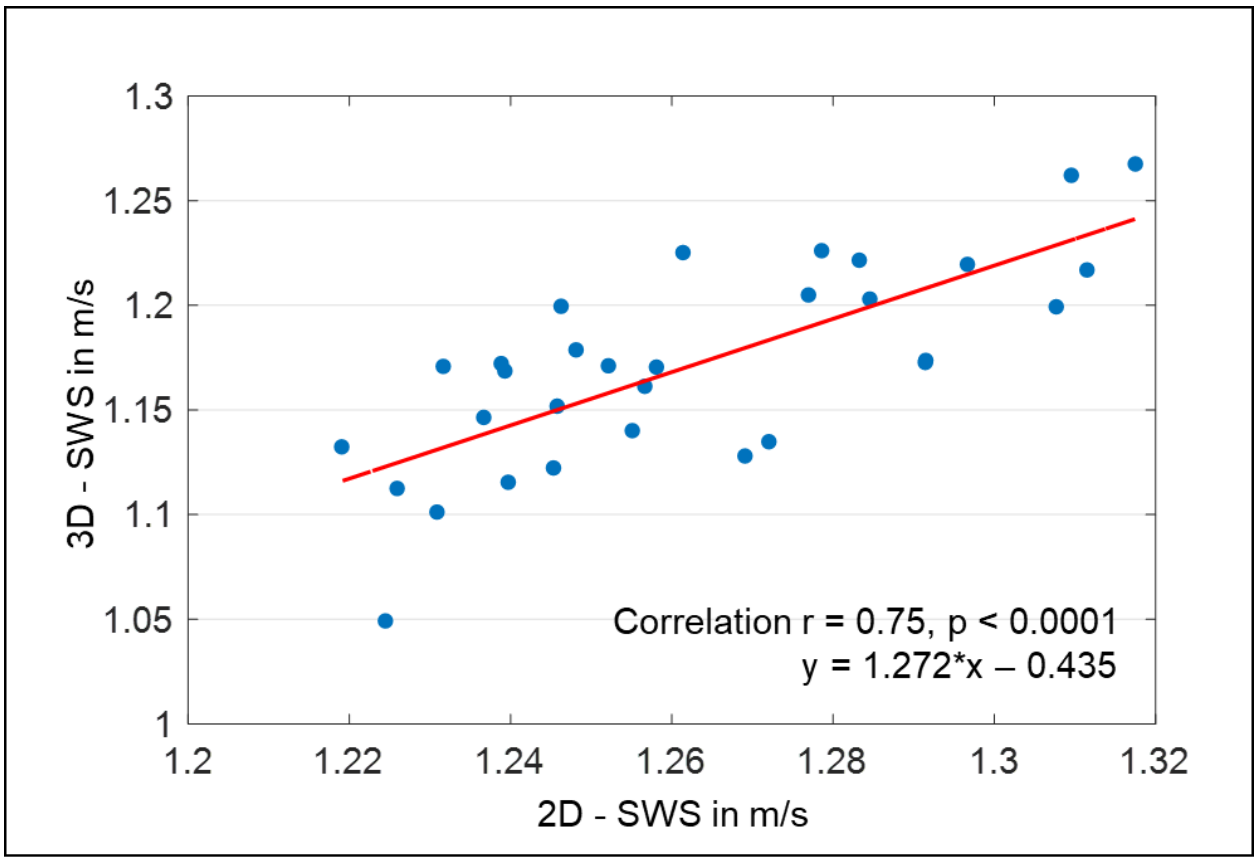

Figure 3: Correlation plot for 2D and 3D SWS values for global brain tissue.

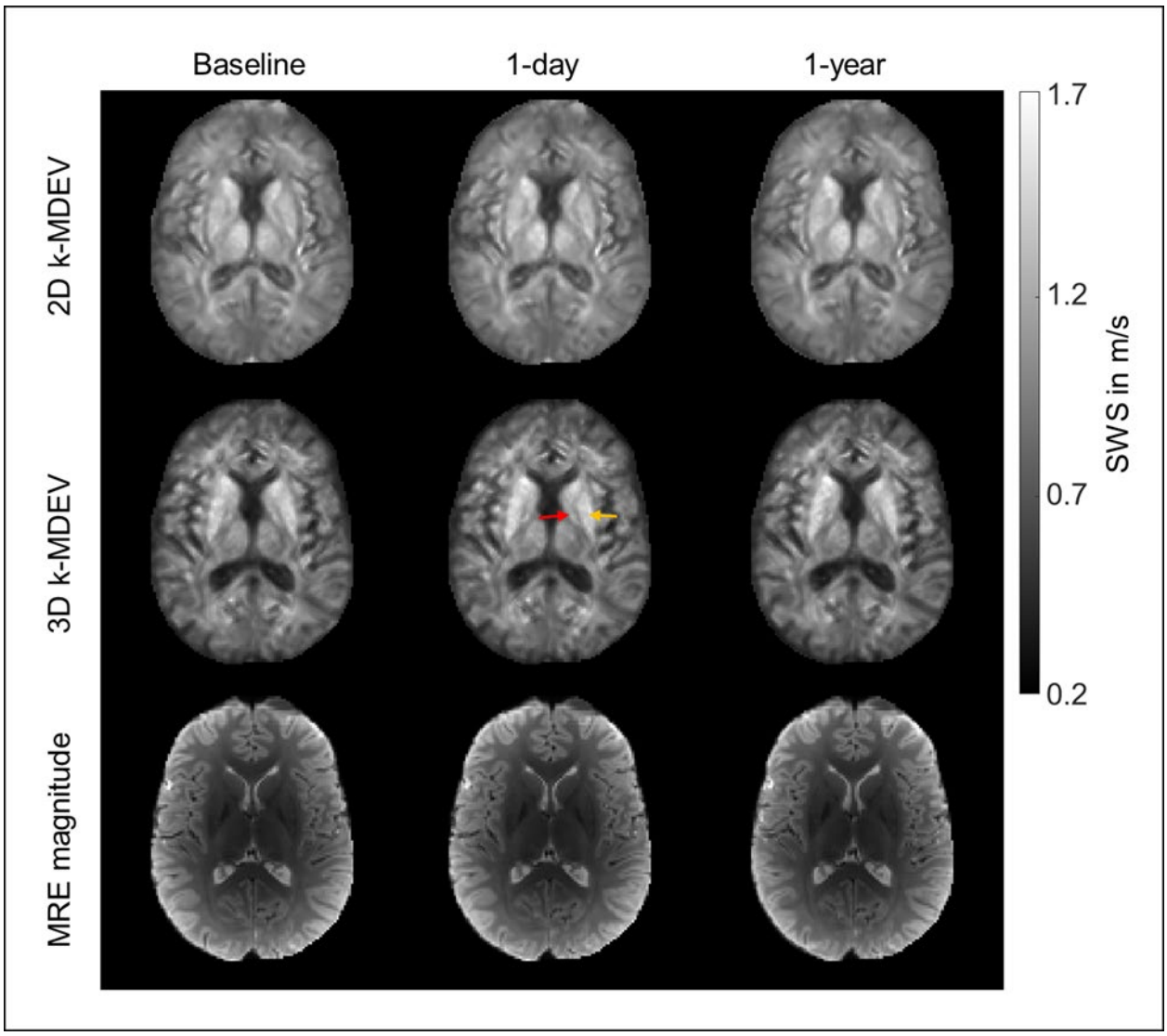

Figure 4: Representative MRE stiffness maps and magnitude images from one volunteer examined at three time points: baseline, one day later (1-day), and one year later (1-year) for 2D (top) and 3D *k*-MDEV-based reconstruction (bottom). The red arrow points to globus pallidus while the yellow arrow points to putamen. Both regions are clearly distinguishable by eye, consistent with distinct group-averaged values.

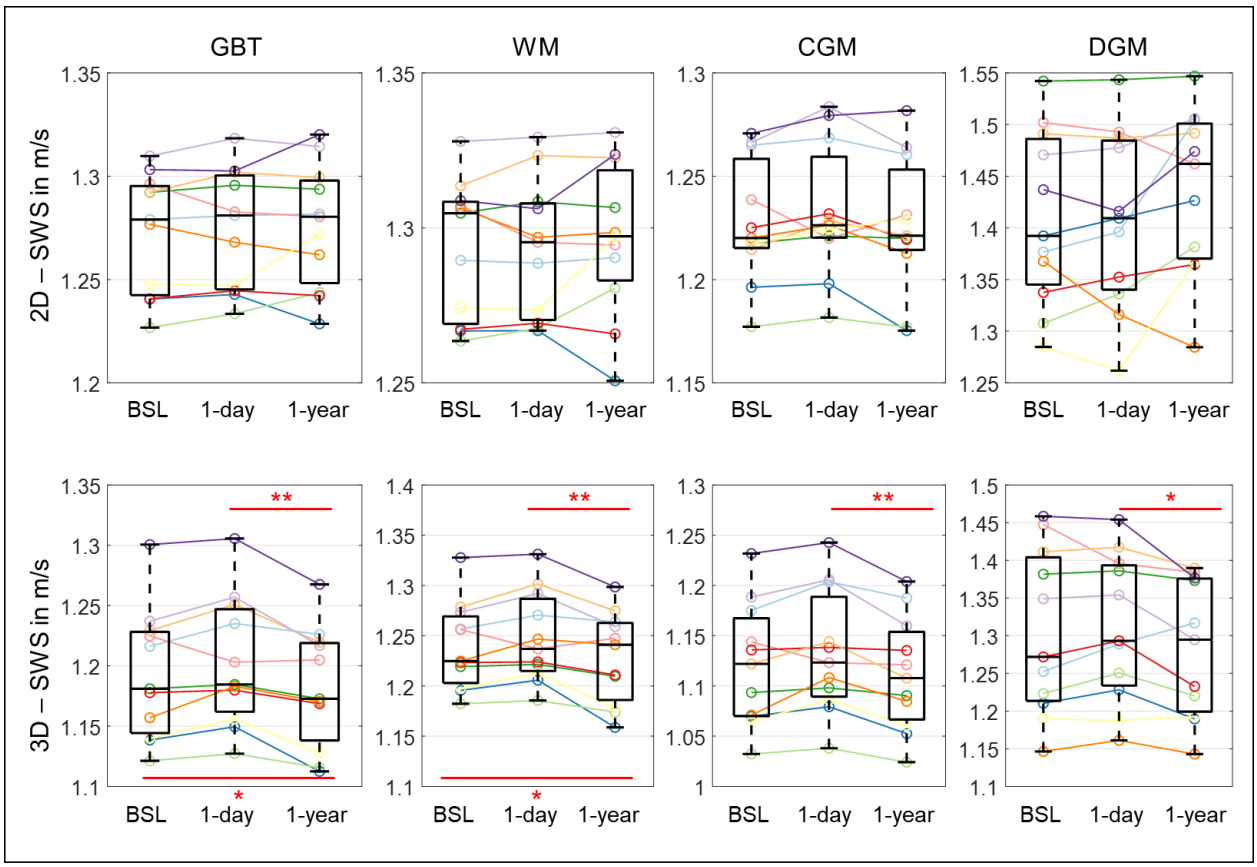

Figure 5: Group-averaged SWS values for 2D (top) and 3D processing (bottom) in global brain tissue (GBT), white matter (WM), cortical gray matter (CGM), and deep gray matter (DGM). Averages were derived from eleven volunteers examined at baseline (BSL), one day later (1-day), and after one year (1-year). Significance levels, indicated by asterisks, were determined from paired t-tests with Holm-Bonferroni correction between BSL and 1-year as well as 1-day and 1-year.

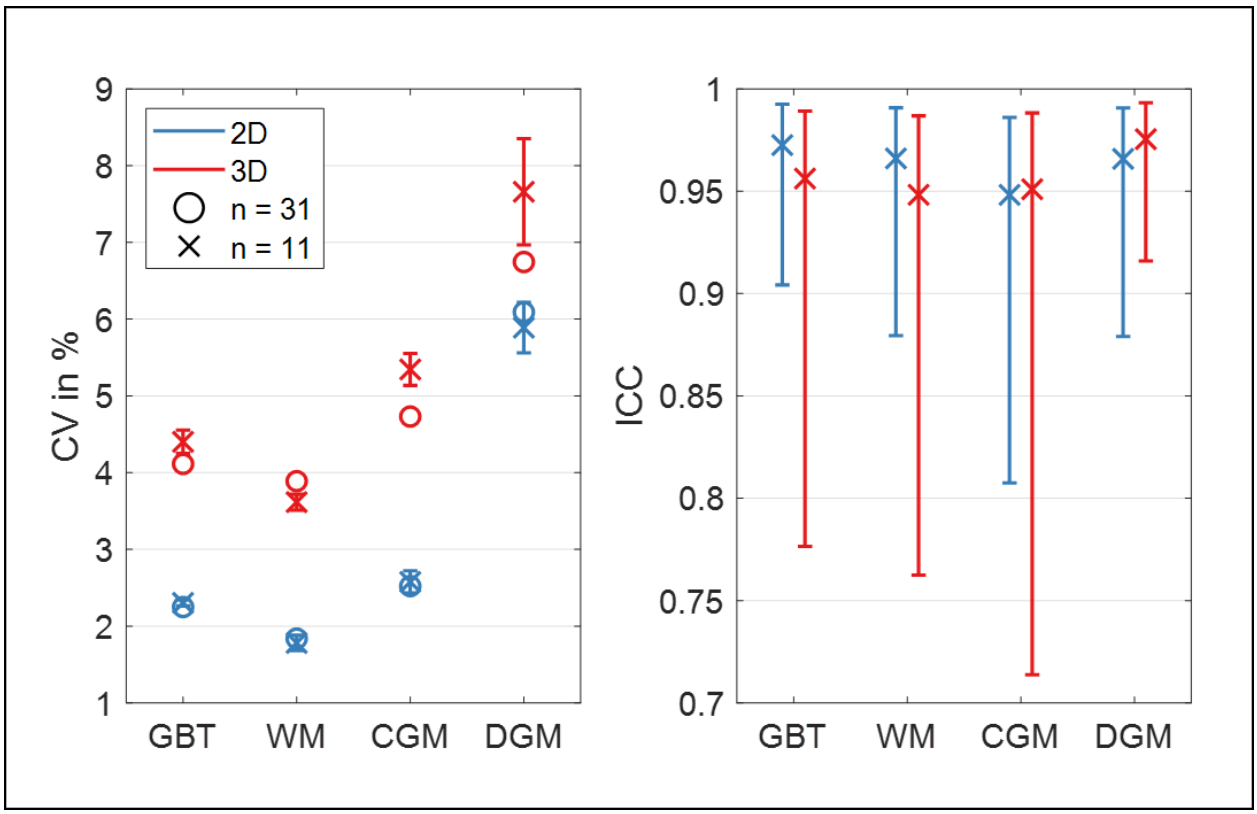

Figure 6: Coefficient of variation (CV, left) and intraclass correlation coefficient (ICC, right) for 2D and 3D SWS reconstructions for global brain tissue (GBT), white matter (WM), cortical gray matter (CGM), and deep gray matter (DGM). CV determined from single examination of all volunteers and as an average from three CVs in eleven volunteers examined at baseline, one day later, and after one year. ICC was determined from baseline and repeated examination after one day.

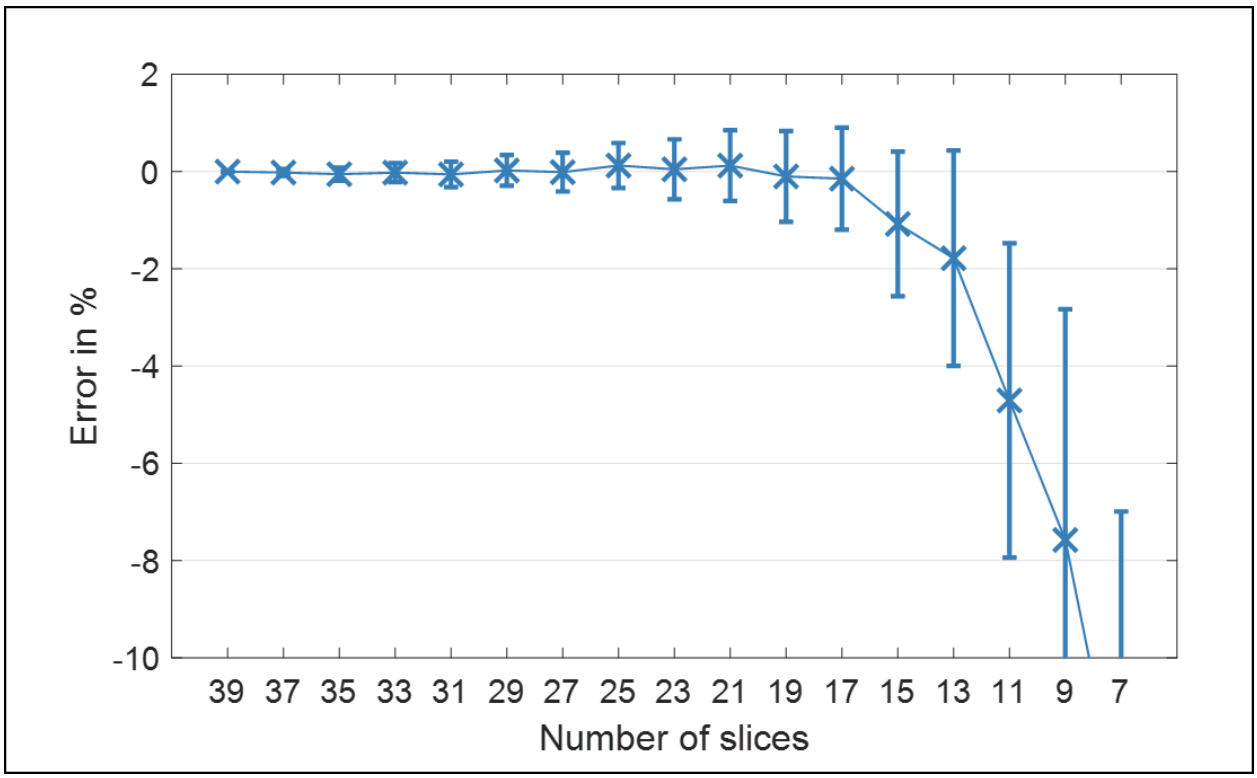

Figure 7: Mean relative error in % for mean white matter SWS using 3D data processing in eleven volunteers. The error is calculated as the relative difference between the reconstructed SWS of the center slice using 39 input slices (reference) and subsequently removing the boundary slices prior to reconstruction.

Discussion

Introducing cerebral tomoelastography, we address the longstanding challenges of brain MRE, namely high variability of values relative to pathophysiological changes and limited anatomical detail in individual MRE maps. To the best of our knowledge, this is the first study which analyzed brain viscoelasticity changes in healthy volunteers after one year. Moreover, we investigated the consistency of MRE parameters by comparing repeated measurement after one day and by comparing 2D and 3D data processing. We also performed a correlation analysis with physiological data, to scrutinize the biological and technical margins of reproducibility of the method. In the following, we discuss the results with regard to SWS.

Strikingly, 2D stiffness values were very similar to 3D values (relative differences <5% in WM and <8% GBT), which we consider an important indication of the overall consistency of the proposed inversion pipeline in addition to excellent reproducibility scores.

Exploring brain mechanics in a frequency range between 20 and 35 Hz, we obtained results that are comparable with previously published values from large-scale dispersion analysis (1.22 – 1.65 m/s for 20 –35 Hz)[48]. Converting our GBT SWS values to the magnitude of the complex shear modulus |G*| using the elastic model (2D-|G*| = 1.6 kPa, 3D-|G*| = 1.4 kPa) facilitates a direct comparison with recently reported values obtained at 50 Hz vibration frequency. Hiscox *et al.*[6] reported GBT |G*| of 2.07 ± 0.42 kPa and 2.62 ± 0.21 kPa[31] while Svensson *et al.*[56] reported storage modulus G' of 1.29 kPa and 1.76 kPa, depending on the inversion algorithm used. Lv *et al.*[57] reported GBT values between 1.6 kPa at 40 Hz and 2.2 kPa at 60 Hz. Yeung *et al.* reported WM |G*| values for healthy adults at 30 and 40 Hz driving frequency of 1.13 ± 0.13 kPa and 1.64 ± 0.19 kPa, respectively.[58] Thus, our mean values are in a range that is covered by the body of the MRE literature.

Similarly, our observation of stiffer DGM than WM (10 – 20%) and softer CGM than WM (5 – 10%) is in agreement with prior research[31], with larger contrasts for 3D. Moreover, in 3D reconstruction, the putamen and globus pallidus were stiffer than the nucleus caudate and thalamus, consistent with Hiscox *et al.*[31], while in 2D, only the putamen was markedly stiffer than other regions. Remarkably, our maps from some volunteers show these anatomical subregions with unprecedented detail and in agreement with standard T2-weighted MR images.

Age-related brain softening, as previously shown by different research groups[7, 8, 59, 60], was reproduced in our cross-sectional study. Converted to |G*|, we found an annual decrease in GBT stiffness of 5 Pa (2D) and 7 Pa (3D), consistent with the average decrease of 8 Pa reported by Hiscox *et al.*[7]. Yet, BPF, which is tightly linked to aging[61], seems to explain most of the age-related changes in GBT SWS. For the first time, we measured annual brain softening due to aging in a test-retest study design. We observed a higher rate of softening when analyzing longitudinal changes with 3D MRE and setting day 0 as reference versus day 1 – 34 Pa versus 49 Pa. Of note, we observed a reduction

of BPF over the course of one year, but we did not observe a reduction of brain tissue volume or any cross-sectional correlation of brain stiffness with other physiological parameters such as BMI and blood pressure during this period. While we observed a positive correlation between BPF and cross-sectional MRE in 2D and 3D, the longitudinal sensitivity of 3D MRE to WM brain softening suggests that MRE is also sensitive to intrinsic brain tissue changes unrelated to brain tissue loss since WM volume did not change. In previous work, we found BMI to be negatively correlated with stiffness in the putamen and globus pallidus[62], two regions which were not addressed by our hypotheses and correlation analyses.

The consistency of cerebral tomoelastography in terms of within-subject (0.33% RAD, 0.95 ICC) and inter-subject (2% CV) variability is encouraging in comparison with other MRE [6, 63, 64] and quantitative MRI techniques [65-67]. For proton density, T1, T2, and T2* relaxation times of WM, Gracien *et al.*[65] reported mean RAD values between 1% and 2% and inter-subject CV values between 2% and 5%. Using diffusion MRI, Heiervang *et al.*[66] reported inter-session CV of fractional anisotropy and mean diffusivity below 5% and 3%, while inter-subject CV was below 10% and 8%, respectively. Quantitative susceptibility mapping [67] and perfusion imaging were found to have correlation coefficients for repeated measurement of r = 0.98, which is considered highly reproducible [68]. Thus, cerebral tomoelastography adds an excellently reproducible and biophysics-based imaging marker to these quantitative MRI methods.

It is worth mentioning that a reproducible setup of our MRE actuator and a reproducible selection of imaging volumes were critical to the high consistency of our values. Therefore, we particularly ensured that the volunteer's head was placed in a similar position on the driver setup during all follow-up examinations, and that the transverse slice blocks were automatically aligned by the scanner. Higher variability with smaller mean values in 3D reconstruction were observed due to noise enhancement by the 3D curl operator and 3D phase gradient calculation, which induces additional through-plane tissue boundary artifacts. Yet, 2D bandpass filtering seemed to blurr small regional stiffness differences (e.g., caudate nucleus versus globus pallidus) and small longitudinal changes such as one-year age effects. Another drawback of 2D MRE is its inability to

account for complex wave propagation patterns including through-slice components.[6, 47] 3D MRE promised to solve this issue, however, it induced boundary slice artifacts, which corrupted up to several boundary slices. Therefore, we cannot fully recommend 3D over 2D MRE, as this study has shown that the influence of boundary slices impoverishes the volume that can be used for unbiased stiffness mapping. For example, we had to exclude 8 out of 40 slices, which is a waste of 20% scan time and spatial information. In addition, as shown in Figure 7, a small number of slices for a given slice block thickness affects the numerical stability of 3D *k*-MDEV inversion, confirming that sample points per wavelength and sampled wavelength fraction influence SWS reconstruction, as previously shown by Mura *et al.*[39].

Our study has limitations. First, the number of volunteers in our longitudinal study was rather small, which precluded tests for multiple confounders that may affect brain stiffness over one year. Therefore, we focused on the effect of aging within one year as the most reproduced and best reported physiological confounder of brain MRE. However, a clear separation of aging effects from loss in BPF was not fully possible. Furthermore, we could not avoid that wave amplitudes varied between individuals even though the technical setup including driver amplitude was identical across all experiments. These amplitude variations are likely due to different head geometries, which affect the efficacy of wave induction. Possibly for that reason, 2D-SWS correlated with wave amplitudes in DGM, which contributed to higher CV values. In the future, variability in brain MRE could be further reduced if wave amplitudes inside the brain were actively controlled using an MRI actuator feedback system. Finally, we focused on frequency compound viscoelasticity maps without in-depth analysis of single frequency data. It would be another interesting and important research question which of the included frequencies in our *k*-MDEV maps contributed most to the variability of our data and how one could further improve the consistency of brain MRE by refinement of the range of vibration frequencies. However, such an analysis would exceed our concise study design. To avoid a lengthy presentation, we confined ourselves to stiffness analysis in the main text while providing the results of viscosity analysis in the supplemental material.

In summary, this study introduced cerebral tomoelastography based on 2D and 3D multifrequency MRE and wavenumber-based multifrequency inversion. We assessed reproducibility, long-term changes, detail resolution, and biological effects on viscoelasticity parameters in the healthy human brain. Our method enabled high-resolution viscoelasticity mapping of anatomical detail as demonstrated by the stiffness-based separation of DGM regions in individual volunteers, which was consistent with group mean values. Stiffness correlated with age and BPF whereas BP and BMI did not correlate with MRE values. Cerebral tomoelastography was highly consistent in terms of CV and ICC, 2D versus 3D, and long-term effects. 2D MRE shows less variation across volunteers and at one-year follow-up than 3D MRE and supports thin imaging slabs while 3D MRE seems to be more sensitive to subtle individual changes such as aging within only one year. Overall, cerebral tomoelastography has shown excellent consistency and detail resolution compared with both classical MRE of the brain and other quantitative MRI techniques. Therefore, it contributes to the quest for reproducible, quantitative, and biophysically significant MRI biomarkers for clinical applications.

Acknowledgments

Funding from the German Research Foundation (GRK 2260 BIOQIC, SFB1340 Matrix in Vision, Sa901/17-2) is gratefully acknowledged.

Declaration of conflicting interests

The authors declare no potential conflicts of interest with respect to the research, authorship, and publication of this article.

Author contributions

Helge Herthum: Conceptualization, Methodology, Software, Validation, Formal analysis, Investigation, Data Curation, Writing - Original Draft, Writing - Review & Editing, Visualization. **Stefan Hetzer:** Conceptualization, Methodology, Validation, Formal analysis, Supervision, Writing - Review & Editing. **Bernhard Kreft:** Methodology, Validation, Formal analysis, Writing - Review & Editing. **Mehrgan Shahryari:** Software, Validation, Formal analysis, Writing - Review & Editing. **Tom Meyer:** Software, Writing -

Review & Editing. **Steffen Görner:** Resources, Writing - Review & Editing. **Hennes Neubauer:** Resources, Writing - Review & Editing. **Jing Guo:** Methodology, Writing - Review & Editing. **Jürgen Braun:** Writing - Review & Editing, Supervision, Project administration, Funding acquisition. **Ingolf Sack:** Conceptualization, Writing - Original Draft, Writing - Review & Editing, Supervision, Project administration, Funding acquisition.

Tables

Table 1: Group mean values of SWS for 2D and 3D data processing and the coefficient of variation (CV) for all analyzed brain regions obtained in 31 brains (cross-sectional study): global brain tissue (GBT), white matter (WM), cortical gray matter (CGM), deep gray matter (DGM), nucleus accumbens (Ac), nucleus caudate (Ca), globus pallidus (Pal), putamen (Pu), and thalamus (Th). Standard deviations are given in brackets. In addition, region size is given.

	2D-SWS in m/s	CV in %	3D-SWS in m/s	CV in %	Size in cm^3
GBT	1.26 (0.03)	2.3	1.17 (0.05)	4.1	909 (44)
WM	1.28 (0.02)	1.8	1.22 (0.05)	3.9	544 (21)
CGM	1.21 (0.03)	2.5	1.09 (0.05)	4.7	379 (22)
DGM	1.42 (0.09)	6.1	1.29 (0.09)	6.7	53 (5)
Ac	1.33 (0.12)	8.7	1.24 (0.10)	7.8	1.6 (0.4)
Ca	1.37 (0.19)	13.5	1.21 (0.19)	16.1	10.1 (0.1)
Pal	1.36 (0.12)	9.1	1.24 (0.11)	8.5	5.5 (0.8)
Pu	1.45 (0.07)	4.7	1.45 (0.08)	5.7	16.5 (1.7)
Th	1.36 (0.10)	7.4	1.11 (0.10)	9.1	26.3 (2.0)

Table 2: Coefficient of variation (CV) and intraclass correlation coefficient (ICC) for 2D and 3D SWS reconstructions for global brain tissue (GBT), white matter (WM), cortical gray matter (CGM), deep gray matter (DGM) and DGM subregions. CV is given as an average of three CVs for baseline, 1-day, and 1-year measurement in eleven volunteers

(n = 11). ICC and mean relative absolute difference (RAD) were determined from baseline and 1-day repeat measurement.

2D SWS	mean CV (SD), n = 11	ICC (95%-CI: low, up)	mean RAD (SD, max) in %
GBT	2.30 (0.04)	0.97 (0.90, 0.99)	0.43 (0.33, 1.04)
WM	1.78 (0.10)	0.97 (0.88, 0.99)	0.33 (0.32, 0.91)
CGM	2.58 (0.14)	0.95 (0.81, 0.99)	0.68 (0.46, 1.51)
DGM	5.89 (0.33)	0.97 (0.88, 0.99)	1.31 (1.06, 3.78)
Ac	7.21 (0.31)	0.98 (0.94, 1)	1.12 (1.12, 0.73)
Ca	14.41 (0.36)	0.99 (0.95, 1)	2.29 (2.29, 1.01)
Pal	8.3 (1.19)	0.96 (0.86, 0.99)	2.18 (2.18, 1.48)
Pu	4.2 (0.17)	0.96 (0.87, 0.99)	1.04 (1.04, 0.59)
Th	8.1 (0.8)	0.97 (0.88, 0.99)	1.59 (1.59, 1.81)
3D SWS	mean CV (SD), n = 11	ICC (95%-CI: low, up)	mean RAD (SD, max) in %
GBT	5.89 (0.33)	0.96 (0.78, 0.99)	1.16 (0.71, 2.25)
WM	3.62 (0.10)	0.95 (0.76, 0.99)	0.96 (0.66, 1.80)
CGM	5.35 (0.21)	0.95 (0.71, 0.99)	1.47 (0.98, 3.49)
DGM	7.66 (0.69)	0.98 (0.92, 0.99)	1.34 (1.17, 3.57)
Ac	6.93 (0.47)	0.92 (0.72, 0.98)	2.48 (2.48, 1.62)
Ca	18.84 (0.63)	0.99 (0.97, 1)	2.04 (2.04, 1.85)
Pal	10.3 (2.06)	0.94 (0.81, 0.98)	3.38 (3.38, 2.34)
Pu	6.04 (0.21)	0.97 (0.88, 0.99)	1.43 (1.43, 0.71)
Th	10.26 (0.99)	0.96 (0.88, 0.99)	2.08 (2.08, 1.8)

Table 3: SWS results of 1-year follow-up examination compared to the baseline and 1-day measurement as references for 3D data processing. Absolute changes in SWS with 95% confidence intervals and Holm-Bonferroni corrected p-values are given for global brain tissue, white matter, cortical gray matter, and deep gray matter.

Region	Parameter	BSL vs 1-year	1-day vs 1-year
Global brain tissue	ΔSWS in m/s	-0.011	-0.021
	95% - CI (low, up)	(-0.020, -0.002)	(-0.030, -0.011)
	p-Value	0.0263	0.0014
White matter	ΔSWS in m/s	-0.011	-0.019
	95% - CI (low, up)	(-0.020, -0.001)	(-0.030, -0.009)
	p-Value	0.0367	0.0068
Cortical gray matter	ΔSWS in m/s	0.009	-0.022
	95% - CI (low, up)	(-0.018, 0.000)	(-0.031, -0.013)
	p-Value	0.0653	0.0012
Deep gray matter	ΔSWS in m/s	0.021	-0.028
	95% - CI (low, up)	(-0.046, 0.004)	(-0.047, -0.008)
	p-Value	0.1098	0.0268

References

[1] S.K. Venkatesh, R.L. Ehman, Magnetic resonance elastography of abdomen, Abdominal imaging 40(4) (2015) 745-59.

[2] Y. Jamin, J.K.R. Boult, J. Li, S. Popov, P. Garteiser, J.L. Ulloa, C. Cummings, G. Box, S.A. Eccles, C. Jones, J.C. Waterton, J.C. Bamber, R. Sinkus, S.P. Robinson, Exploring the biomechanical properties of brain malignancies and their pathologic determinants in vivo with magnetic resonance elastography, Cancer Res 75(7) (2015) 1216-1224.

[3] M.C. Murphy, J. Huston, 3rd, R.L. Ehman, MR elastography of the brain and its application in neurological diseases, Neuroimage 187 (2019) 176-183.

[4] S. Hirsch, J. Braun, I. Sack, Magnetic Resonance Elastography: Physical Background And Medical Applications, Wiley-VCH2017.
[5] Z. Yin, A.J. Romano, A. Manduca, R.L. Ehman, J. Huston, 3rd, Stiffness and Beyond: What MR Elastography Can Tell Us About Brain Structure and Function Under Physiologic and Pathologic Conditions, Top Magn Reson Imaging 27(5) (2018) 305-318.
[6] L.V. Hiscox, C.L. Johnson, E. Barnhill, M.D. McGarry, J. Huston, E.J. van Beek, J.M. Starr, N. Roberts, Magnetic resonance elastography (MRE) of the human brain: technique, findings and clinical applications, Phys Med Biol 61(24) (2016) R401-R437.
[7] L.V. Hiscox, H. Schwarb, M.D.J. McGarry, C.L. Johnson, Aging brain mechanics: Progress and promise of magnetic resonance elastography, Neuroimage 232 (2021) 117889.
[8] I. Sack, B. Beierbach, J. Wuerfel, D. Klatt, U. Hamhaber, S. Papazoglou, P. Martus, J. Braun, The impact of aging and gender on brain viscoelasticity, Neuroimage 46(3) (2009) 652-7.
[9] A. Arani, M.C. Murphy, K.J. Glaser, A. Manduca, D.S. Lake, S.A. Kruse, C.R. Jack, Jr., R.L. Ehman, J. Huston, 3rd, Measuring the effects of aging and sex on regional brain stiffness with MR elastography in healthy older adults, Neuroimage 111 (2015) 59-64.
[10] L.V. Hiscox, C.L. Johnson, M.D.J. McGarry, H. Marshall, C.W. Ritchie, E.J.R. van Beek, N. Roberts, J.M. Starr, Mechanical property alterations across the cerebral cortex due to Alzheimer's disease, Brain Commun 2(1) (2020) fcz049.
[11] M.C. Murphy, D.T. Jones, C.R. Jack, Jr., K.J. Glaser, M.L. Senjem, A. Manduca, J.P. Felmlee, R.E. Carter, R.L. Ehman, J. Huston, 3rd, Regional brain stiffness changes across the Alzheimer's disease spectrum, Neuroimage Clin 10 (2016) 283-90.
[12] M.C. Murphy, J. Huston, 3rd, C.R. Jack, K.J. Glaser, A. Manduca, J.P. Felmlee, R.L. Ehman, Decreased Brain Stiffness in Alzheimer's Disease Determined by Magnetic Resonance Elastography, Proceedings 19th Scientific Meeting, International Society for Magnetic Resonance in Medicine, Montreal, 2011, p. 690.
[13] J. Wuerfel, F. Paul, B. Beierbach, U. Hamhaber, D. Klatt, S. Papazoglou, F. Zipp, P. Martus, J. Braun, I. Sack, MR-elastography reveals degradation of tissue integrity in multiple sclerosis, Neuroimage 49(3) (2010) 2520-5.

[14] A. Fehlner, J.R. Behrens, K.J. Streitberger, S. Papazoglou, J. Braun, J. Bellmann-Strobl, K. Ruprecht, F. Paul, J. Wurfel, I. Sack, Higher-resolution MR elastography reveals early mechanical signatures of neuroinflammation in patients with clinically isolated syndrome, J Magn Reson Imaging 44(1) (2016) 51-8.
[15] A. Lipp, C. Skowronek, A. Fehlner, K.J. Streitberger, J. Braun, I. Sack, Progressive supranuclear palsy and idiopathic Parkinson's disease are associated with local reduction of in vivo brain viscoelasticity, Eur Radiol 28(8) (2018) 3347-3354.
[16] A. Lipp, R. Trbojevic, F. Paul, A. Fehlner, S. Hirsch, M. Scheel, C. Noack, J. Braun, I. Sack, Cerebral magnetic resonance elastography in supranuclear palsy and idiopathic Parkinson's disease, Neuroimage Clin 3 (2013) 381-7.
[17] F.B. Freimann, K.J. Streitberger, D. Klatt, K. Lin, J. McLaughlin, J. Braun, C. Sprung, I. Sack, Alteration of brain viscoelasticity after shunt treatment in normal pressure hydrocephalus, Neuroradiology 54(3) (2012) 189-96.
[18] K.J. Streitberger, E. Wiener, J. Hoffmann, F.B. Freimann, D. Klatt, J. Braun, K. Lin, J. McLaughlin, C. Sprung, R. Klingebiel, I. Sack, In vivo viscoelastic properties of the brain in normal pressure hydrocephalus, NMR Biomed 24(4) (2011) 385-92.
[19] A. Hatt, S. Cheng, K. Tan, R. Sinkus, L.E. Bilston, MR Elastography Can Be Used to Measure Brain Stiffness Changes as a Result of Altered Cranial Venous Drainage During Jugular Compression, AJNR Am J Neuroradiol 36(10) (2015) 1971-7.
[20] H. Herthum, M. Shahryari, H. Tzschatzsch, F. Schrank, C. Warmuth, S. Gorner, S. Hetzer, H. Neubauer, J. Pfeuffer, J. Braun, I. Sack, Real-Time Multifrequency MR Elastography of the Human Brain Reveals Rapid Changes in Viscoelasticity in Response to the Valsalva Maneuver, Front Bioeng Biotechnol 9(335) (2021) 666456.
[21] S. Hetzer, F. Dittmann, K. Bormann, S. Hirsch, A. Lipp, D.J. Wang, J. Braun, I. Sack, Hypercapnia increases brain viscoelasticity, J Cereb Blood Flow Metab 39(12) (2019) 2445-2455.
[22] S. Hetzer, P. Birr, A. Fehlner, S. Hirsch, F. Dittmann, E. Barnhill, J. Braun, I. Sack, Perfusion alters stiffness of deep gray matter, J Cereb Blood Flow Metab 38(1) (2018) 116-125.

[23] B. Kreft, H. Tzschatzsch, F. Schrank, J. Bergs, K.J. Streitberger, S. Waldchen, S. Hetzer, J. Braun, I. Sack, Time-Resolved Response of Cerebral Stiffness to Hypercapnia in Humans, Ultrasound Med Biol 46(4) (2020) 936-943.
[24] S. Patz, D. Fovargue, K. Schregel, N. Nazari, M. Palotai, P.E. Barbone, B. Fabry, A. Hammers, S. Holm, S. Kozerke, D. Nordsletten, R. Sinkus, Imaging localized neuronal activity at fast time scales through biomechanics, Sci Adv 5(4) (2019) eaav3816.
[25] P.S. Lan, K.J. Glaser, R.L. Ehman, G.H. Glover, Imaging brain function with simultaneous BOLD and viscoelasticity contrast: fMRI/fMRE, Neuroimage 211 (2020) 116592.
[26] L.M. Gerischer, A. Fehlner, T. Kobe, K. Prehn, D. Antonenko, U. Grittner, J. Braun, I. Sack, A. Floel, Combining viscoelasticity, diffusivity and volume of the hippocampus for the diagnosis of Alzheimer's disease based on magnetic resonance imaging, Neuroimage Clin 18 (2018) 485-493.
[27] K.J. Streitberger, I. Sack, D. Krefting, C. Pfuller, J. Braun, F. Paul, J. Wuerfel, Brain viscoelasticity alteration in chronic-progressive multiple sclerosis, PloS one 7(1) (2012) e29888.
[28] A. Bunevicius, K. Schregel, R. Sinkus, A. Golby, S. Patz, REVIEW: MR elastography of brain tumors, Neuroimage Clin 25 (2020) 102109.
[29] M. Simon, J. Guo, S. Papazoglou, H. Scholand-Engler, C. Erdmann, U. Melchert, M. Bonsanto, J. Braun, D. Petersen, I. Sack, J. Wuerfel, Non-invasive characterization of intracranial tumors by MR-Elastography, The New Journal of Physics 15 (2013) 085024.
[30] H. Herthum, S. Hetzer, M. Scheel, M. Shahryari, J. Braun, F. Paul, I. Sack, In vivo stiffness of multiple sclerosis lesions is similar to that of normal-appearing white matter, Acta Biomater 138 (2022) 410-421.
[31] L.V. Hiscox, M.D.J. McGarry, H. Schwarb, E.E.W. Van Houten, R.T. Pohlig, N. Roberts, G.R. Huesmann, A.Z. Burzynska, B.P. Sutton, C.H. Hillman, A.F. Kramer, N.J. Cohen, A.K. Barbey, K.D. Paulsen, C.L. Johnson, Standard-space atlas of the viscoelastic properties of the human brain, Hum Brain Mapp 41(18) (2020) 5282-5300.
[32] J. Guo, S. Hirsch, A. Fehlner, S. Papazoglou, M. Scheel, J. Braun, I. Sack, Towards an elastographic atlas of brain anatomy, PloS one 8(8) (2013) e71807.

[33] M.C. Murphy, J. Huston, 3rd, C.R. Jack, Jr., K.J. Glaser, M.L. Senjem, J. Chen, A. Manduca, J.P. Felmlee, R.L. Ehman, Measuring the characteristic topography of brain stiffness with magnetic resonance elastography, PloS one 8(12) (2013) e81668.
[34] J. Guo, S. Hirsch, S. Papazoglou, A. Fehlner, M. Scheel, J. Wuerfel, I. Sack, J. Braun, An atlas of the anatomy of human brain viscoelasticity, in: I.P.o.t.s.A.M.o. ISMRM (Ed.) Proc 21st Annual Meeting ISMRM, Salt Lake City, 2013.
[35] F. Dittmann, S. Hirsch, H. Tzschatzsch, J. Guo, J. Braun, I. Sack, In vivo wideband multifrequency MR elastography of the human brain and liver, Magn Reson Med 76(4) (2016) 1116-26.
[36] A. Romano, M. Scheel, S. Hirsch, J. Braun, I. Sack, In vivo waveguide elastography of white matter tracts in the human brain, Magn Reson Med 68(5) (2012) 1410-22.
[37] A. Manduca, T.L. Rossman, D.S. Lake, K.J. Glaser, A. Arani, S.P. Arunachalam, P.J. Rossman, J.D. Trzasko, R.L. Ehman, D. Dragomir-Daescu, P.A. Araoz, Waveguide effects and implications for cardiac magnetic resonance elastography: A finite element study, NMR Biomed (2018) e3996.
[38] H. Tzschatzsch, J. Guo, F. Dittmann, S. Hirsch, E. Barnhill, K. Johrens, J. Braun, I. Sack, Tomoelastography by multifrequency wave number recovery from time-harmonic propagating shear waves, Med Image Anal 30 (2016) 1-10.
[39] J. Mura, F. Schrank, I. Sack, An analytical solution to the dispersion-by-inversion problem in magnetic resonance elastography, Magn Reson Med 84(1) (2020) 61-71.
[40] F. Dittmann, H. Tzschatzsch, S. Hirsch, E. Barnhill, J. Braun, I. Sack, J. Guo, Tomoelastography of the abdomen: Tissue mechanical properties of the liver, spleen, kidney, and pancreas from single MR elastography scans at different hydration states, Magn Reson Med 78(3) (2017) 976-983.
[41] M. Shahryari, H. Tzschatzsch, J. Guo, S.R. Marticorena Garcia, G. Boning, U. Fehrenbach, L. Stencel, P. Asbach, B. Hamm, J.A. Kas, J. Braun, T. Denecke, I. Sack, Tomoelastography Distinguishes Noninvasively between Benign and Malignant Liver Lesions, Cancer Res 79(22) (2019) 5704-5710.
[42] R. Reiter, H. Tzschatzsch, F. Schwahofer, M. Haas, C. Bayerl, M. Muche, D. Klatt, S. Majumdar, M. Uyanik, B. Hamm, J. Braun, I. Sack, P. Asbach, Diagnostic performance

of tomoelastography of the liver and spleen for staging hepatic fibrosis, Eur Radiol 30(3) (2020) 1719-1729.
[43] W.D. Penny, K.J. Friston, J.T. Ashburner, S.J. Kiebel, T.E. Nichols, Statistical parametric mapping: the analysis of functional brain images, Elsevier2011.
[44] F. Schrank, C. Warmuth, H. Tzschatzsch, B. Kreft, S. Hirsch, J. Braun, T. Elgeti, I. Sack, Cardiac-gated steady-state multifrequency magnetic resonance elastography of the brain: Effect of cerebral arterial pulsation on brain viscoelasticity, J Cereb Blood Flow Metab 40(5) (2020) 991-1001.
[45] M.A. Griswold, P.M. Jakob, R.M. Heidemann, M. Nittka, V. Jellus, J. Wang, B. Kiefer, A. Haase, Generalized autocalibrating partially parallel acquisitions (GRAPPA), Magn Reson Med 47(6) (2002) 1202-10.
[46] J. Mazziotta, A. Toga, A. Evans, P. Fox, J. Lancaster, K. Zilles, R. Woods, T. Paus, G. Simpson, B. Pike, C. Holmes, L. Collins, P. Thompson, D. MacDonald, M. Iacoboni, T. Schormann, K. Amunts, N. Palomero-Gallagher, S. Geyer, L. Parsons, K. Narr, N. Kabani, G. Le Goualher, J. Feidler, K. Smith, D. Boomsma, H. Hulshoff Pol, T. Cannon, R. Kawashima, B. Mazoyer, A four-dimensional probabilistic atlas of the human brain, J Am Med Inform Assoc 8(5) (2001) 401-30.
[47] A. Manduca, P.J. Bayly, R.L. Ehman, A. Kolipaka, T.J. Royston, I. Sack, R. Sinkus, B.E. Van Beers, MR elastography: Principles, guidelines, and terminology, Magn Reson Med 85(5) (2021) 2377-2390.
[48] H. Herthum, S.C.H. Dempsey, A. Samani, F. Schrank, M. Shahryari, C. Warmuth, H. Tzschätzsch, J. Braun, I. Sack, Superviscous properties of the in vivo brain at large scales, Acta Biomater 121 (2021) 393-404.
[49] H. Herthum, H. Tzschätzsch, T. Meyer, M. Shahryari, L. Stencel, J. Guo, J. Braun, I. Sack, Magnetic resonance elastography of the in vivo human brain using multifrequency wavenumber analysis in 2D and 3D., in: I.P.o.t.s.A.M.o. ISMRM (Ed.) ISMRM & SMRT Virtual Conference & Exhibition, 2021.
[50] T. Meyer, S. Marticorena Garcia, H. Tzschatzsch, H. Herthum, M. Shahryari, L. Stencel, J. Braun, P. Kalra, A. Kolipaka, I. Sack, Comparison of inversion methods in MR elastography: An open-access pipeline for processing multifrequency shear-wave data and demonstration in a phantom, human kidneys, and brain, Magn Reson Med (2022).

[51] E. Barnhill, M. Nikolova, C. Ariyurek, F. Dittmann, J. Braun, I. Sack, Fast Robust Dejitter and Interslice Discontinuity Removal in MRI Phase Acquisitions: Application to Magnetic Resonance Elastography, IEEE Trans Med Imaging 38(7) (2019) 1578-1587.
[52] J.M. Bland, D.G. Altman, Applying the right statistics: analyses of measurement studies, Ultrasound Obstet Gynecol 22(1) (2003) 85-93.
[53] M. Bédard, N.J. Martin, P. Krueger, K. Brazil, Assessing reproducibility of data obtained with instruments based on continuous measurements, Exp Aging Res 26(4) (2000) 353-65.
[54] B.S. Everitt, D.C. Howell, Encyclopedia of Statistics in Behavioral Science–Volume 2, John Wiley & Sons, Ltd2021.
[55] L. Lilaj, H. Herthum, T. Meyer, M. Shahryari, G. Bertalan, A. Caiazzo, J. Braun, T. Fischer, S. Hirsch, I. Sack, Inversion-recovery MR elastography of the human brain for improved stiffness quantification near fluid-solid boundaries, Magn Reson Med 86(5) (2021) 2552-2561.
[56] S.F. Svensson, J. De Arcos, O.I. Darwish, J. Fraser-Green, T.H. Storas, S. Holm, E.O. Vik-Mo, R. Sinkus, K.E. Emblem, Robustness of MR Elastography in the Healthy Brain: Repeatability, Reliability, and Effect of Different Reconstruction Methods, J Magn Reson Imaging 53(5) (2021) 1510-1521.
[57] H. Lv, M. Kurt, N. Zeng, E. Ozkaya, F. Marcuz, L. Wu, K. Laksari, D.B. Camarillo, K.B. Pauly, Z. Wang, M. Wintermark, MR elastography frequency-dependent and independent parameters demonstrate accelerated decrease of brain stiffness in elder subjects, Eur Radiol 30(12) (2020) 6614-6623.
[58] J. Yeung, L. Juge, A. Hatt, L.E. Bilston, Paediatric brain tissue properties measured with magnetic resonance elastography, Biomech Model Mechanobiol 18(5) (2019) 1497-1505.
[59] E. Barnhill, P.J. Davies, C. Ariyurek, A. Fehlner, J. Braun, I. Sack, Heterogeneous Multifrequency Direct Inversion (HMDI) for magnetic resonance elastography with application to a clinical brain exam, Med Image Anal 46 (2018) 180-188.
[60] I. Sack, K.J. Streitberger, D. Krefting, F. Paul, J. Braun, The influence of physiological aging and atrophy on brain viscoelastic properties in humans, PloS one 6(9) (2011) e23451.

[61] R. Peters, Ageing and the brain, Postgrad Med J 82(964) (2006) 84-8.
[62] S. Hetzer, S. Hirsch, J. Braun, I. Sack, M. Weygandt, Viscoelasticity of striatal brain areas reflects variations in body mass index of lean to overweight male adults, Brain Imaging Behav 14(6) (2020) 2477-2487.
[63] X. Huang, H. Chafi, K.L. Matthews, 2nd, O. Carmichael, T. Li, Q. Miao, S. Wang, G. Jia, Magnetic resonance elastography of the brain: A study of feasibility and reproducibility using an ergonomic pillow-like passive driver, Magn Reson Imaging 59 (2019) 68-76.
[64] C.L. Johnson, H. Schwarb, D.J.M. M, A.T. Anderson, G.R. Huesmann, B.P. Sutton, N.J. Cohen, Viscoelasticity of subcortical gray matter structures, Hum Brain Mapp 37(12) (2016) 4221-4233.
[65] R.M. Gracien, M. Maiworm, N. Bruche, M. Shrestha, U. Noth, E. Hattingen, M. Wagner, R. Deichmann, How stable is quantitative MRI? - Assessment of intra- and inter-scanner-model reproducibility using identical acquisition sequences and data analysis programs, Neuroimage 207 (2020) 116364.
[66] E. Heiervang, T.E. Behrens, C.E. Mackay, M.D. Robson, H. Johansen-Berg, Between session reproducibility and between subject variability of diffusion MR and tractography measures, Neuroimage 33(3) (2006) 867-77.
[67] K. Deh, T.D. Nguyen, S. Eskreis-Winkler, M.R. Prince, P. Spincemaille, S. Gauthier, I. Kovanlikaya, Y. Zhang, Y. Wang, Reproducibility of quantitative susceptibility mapping in the brain at two field strengths from two vendors, J Magn Reson Imaging 42(6) (2015) 1592-600.
[68] C. Granziera, J. Wuerfel, F. Barkhof, M. Calabrese, N. De Stefano, C. Enzinger, N. Evangelou, M. Filippi, J.J.G. Geurts, D.S. Reich, M.A. Rocca, S. Ropele, A. Rovira, P. Sati, A.T. Toosy, H. Vrenken, C.A.M. Gandini Wheeler-Kingshott, L. Kappos, M.S. Group, Quantitative magnetic resonance imaging towards clinical application in multiple sclerosis, Brain 144(5) (2021) 1296-1311.

Supplementary material to

Cerebral tomoelastography based on multifrequency MR elastography in two and three dimensions.

Helge Herthum[1], Stefan Hetzer[2], Bernhard Kreft[3], Heiko Tzschätzsch[3], Mehrgan Shahryari[3], Tom Meyer[3], Steffen Görner[3], Hennes Neubauer[3], Jing Guo[3], Jürgen Braun[1], Ingolf Sack[3]*

[1]Institute of Medical Informatics, Charité – Universitätsmedizin Berlin, Corporate Member of Freie Universität Berlin, Humboldt-Universität zu Berlin, and Berlin Institute of Health, 10117, Berlin, Germany
[2]Berlin Center for Advanced Neuroimaging (BCAN), 10117, Berlin, Germany
[3]Department of Radiology, Charité – Universitätsmedizin Berlin, Corporate Member of Freie Universität Berlin, Humboldt-Universität zu Berlin, and Berlin Institute of Health, 10117, Berlin, Germany

*__Corresponding author:__

Ingolf Sack, PhD
Department of Radiology
Charité – Universitätsmedizin Berlin
Charitéplatz 1
10117 Berlin, Germany
Tel +49 30 450 539058
Ingolf.sack@charite.de

We here present a complementary data analysis for the penetration rate PR reconstructed using the wavenumber-based (*k*-)MDEV inversion.

Supplementary Figure 1 shows three representative slices in MNI space of group averaged PR generated by 2D and 3D processing along with anatomical reference images from the MNI atlas. Masks for WM, CGM and DGM, after the exclusion of

cerebrospinal fluid, are demarcated by colored lines. A descriptive summary for all analyzed regions is given in Supplementary Table 1, including region size and CV.

Group statistical plots for GBT, WM, CGM and DGM in 2D and 3D are shown in Supplementary Figure 2. Mean WM PR values were markedly higher for 2D (0.83 ± 0.04 m/s) than 3D processing (0.56 ± 0.03 m/s, $p < 0.0001$). PR was significantly lower in CGM and DGM for 2D reconstruction (CGM: 0.82 ± 0.05 m/s, DGM: 0.77 ± 0.1 m/s, $p < 0.0001$ for each test). For 3D reconstruction, PR was significantly lower in CGM (0.55 ± 0.03 m/s, $p < 0.0001$) and significantly higher in DGM (0.6 ± 0.04 m/s, $p < 0.0001$). A descriptive summary for all analyzed regions is given in Supplementary Table 1, including region size and CV. Intersubject variations as quantified by CV were smaller in 2D than 3D processing. CV in GBT, WM, CGM and DGM was 5.4%, 4.8%, 6.1% and 12.6% in 2D MRE while 4.4%, 3.8%, 5.9% and 6.9% in 3D MRE, respectively (see also Supplementary Figure 6). Supplementary Figure 3 shows a correlation plot for 2D and 3D PR values for GBT. The results for both approaches were highly correlated ($r = 0.74$, $p < 0.0001$).

2D PR was positively correlated with wave amplitudes in the respective region (GBT: $r = 0.74$, $p < 0.0001$, WM: $r = 0.73$, $p < 0.0001$). 3D PR was positively correlated with BPF (GBT: $r = 0.45$, $p = 0.043$) and wave amplitudes in the respective region (GBT: $r = 0.49$, $p = 0.024$, CGM: $r = 0.46$, $p = 0.037$, DGM: $r = 0.65$, $p = 0.0004$).

Supplementary Figure 4 shows the reconstructed PR map in a representative slice from one subject for three measurements: baseline, one day later and after one year for both 2D and 3D processing. No differences between the three measurements were visually apparent. Group averaged PR values (2D and 3D for GBT, WM, CGM, DGM) measured at three time points in eleven subjects are presented in Supplementary Figure 5. Intersubject variability assessed by CV, as well as reproducibility between baseline and one day later assessed by ICC and mean RAD (within subject variability) were derived from these results and displayed in Supplementary Figure 6. Supplementary Tables 2 summarizes the one-day test-retest and one-year follow-up results, respectively. Supplementary Figure 6 shows CV values for 2D and 3D data processing based on all subjects and as an average of individual CVs from baseline, 1-day and 1-year measurements for eleven subjects. A summary for CV, ICC and RAD is given in

Supplementary Table 2. Supplementary Figure 7 demonstrates how 3D PR averaged within WM of the center slice is affected by the total number of input slices for a fixed block thickness.

PR in GBT was roughly 33% lower in 3D than 2D. These differences are likely due to the noise enhancing curl operator which has a stronger effect on the calculation of PR.

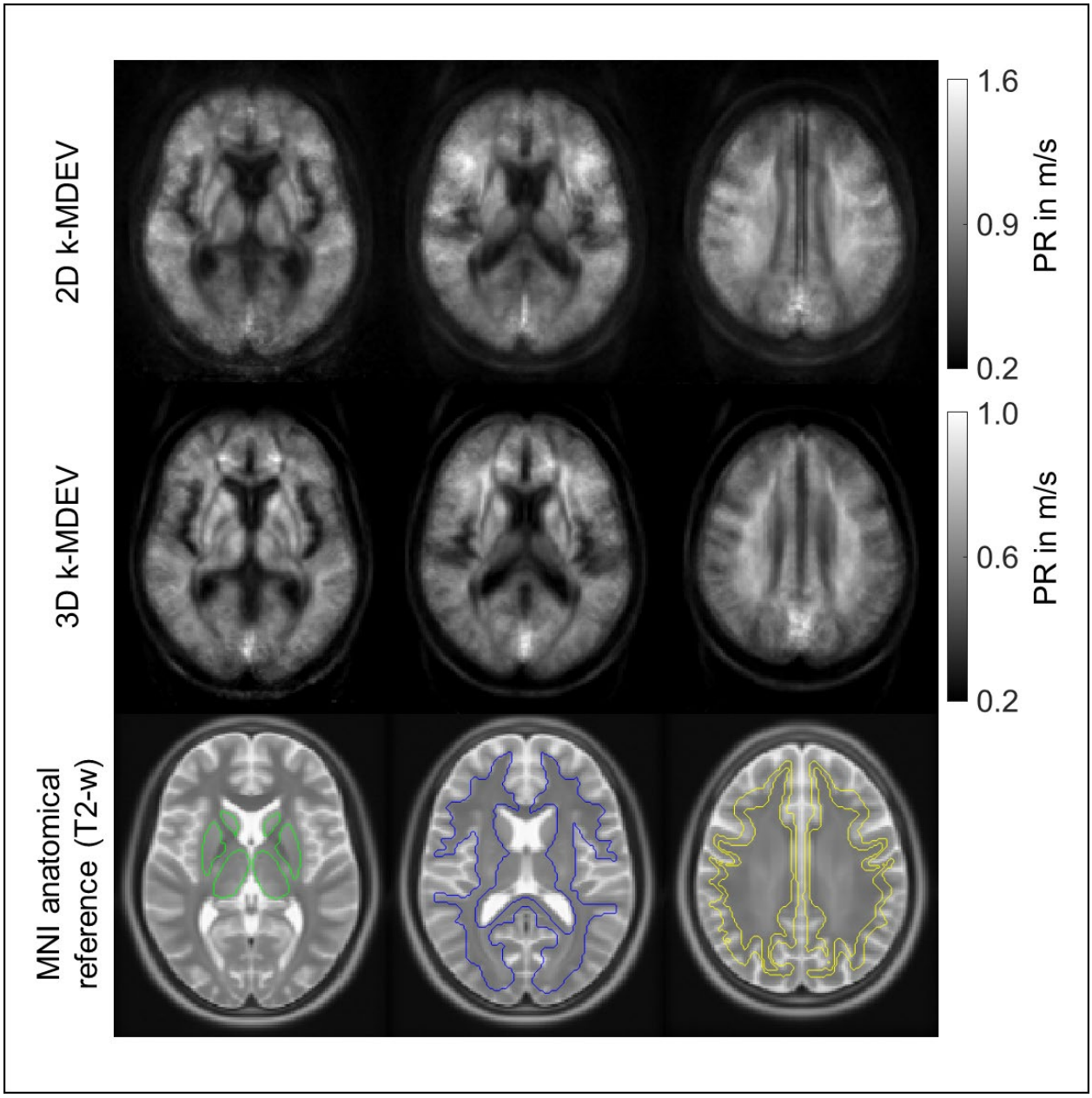

Supplementary Figure 1: Averaged PR maps from 2D and 3D *k*-MDEV inversions normalized to MNI space in three representative slices. Anatomical reference images are

shown superimposed with atlas regions for deep gray matter (green), white matter (blue) and cortical gray matter (yellow).

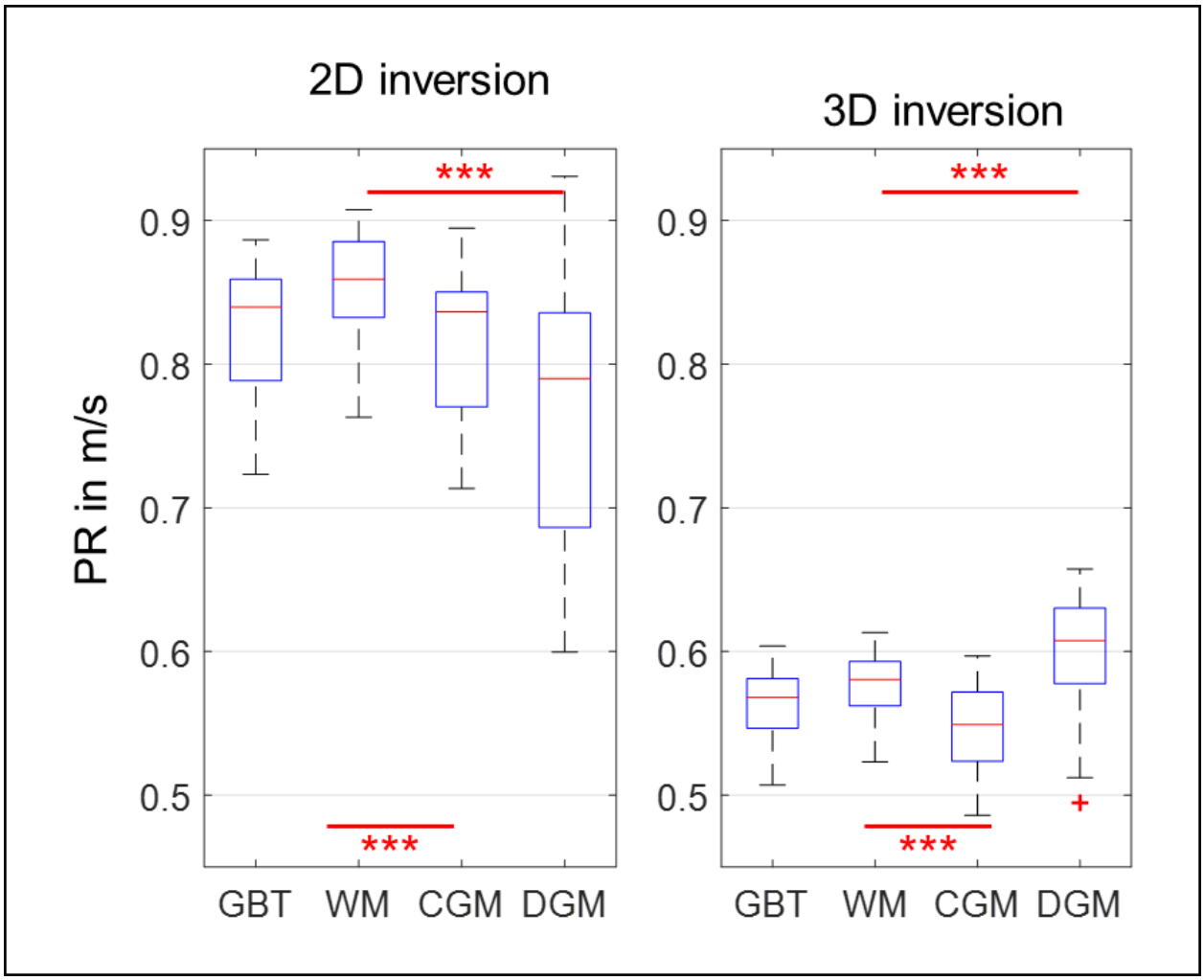

Supplementary Figure 2: Group mean PR values for 2D and 3D *k*-MDEV for global brain tissue (GBT), white matter (WM), cortical gray matter (CGM) and deep gray matter (DGM). Significance levels, indicated by asterisks, were determined from paired t-tests with Holm-Bonferroni correction between WM and CGM as well as WM and DGM.

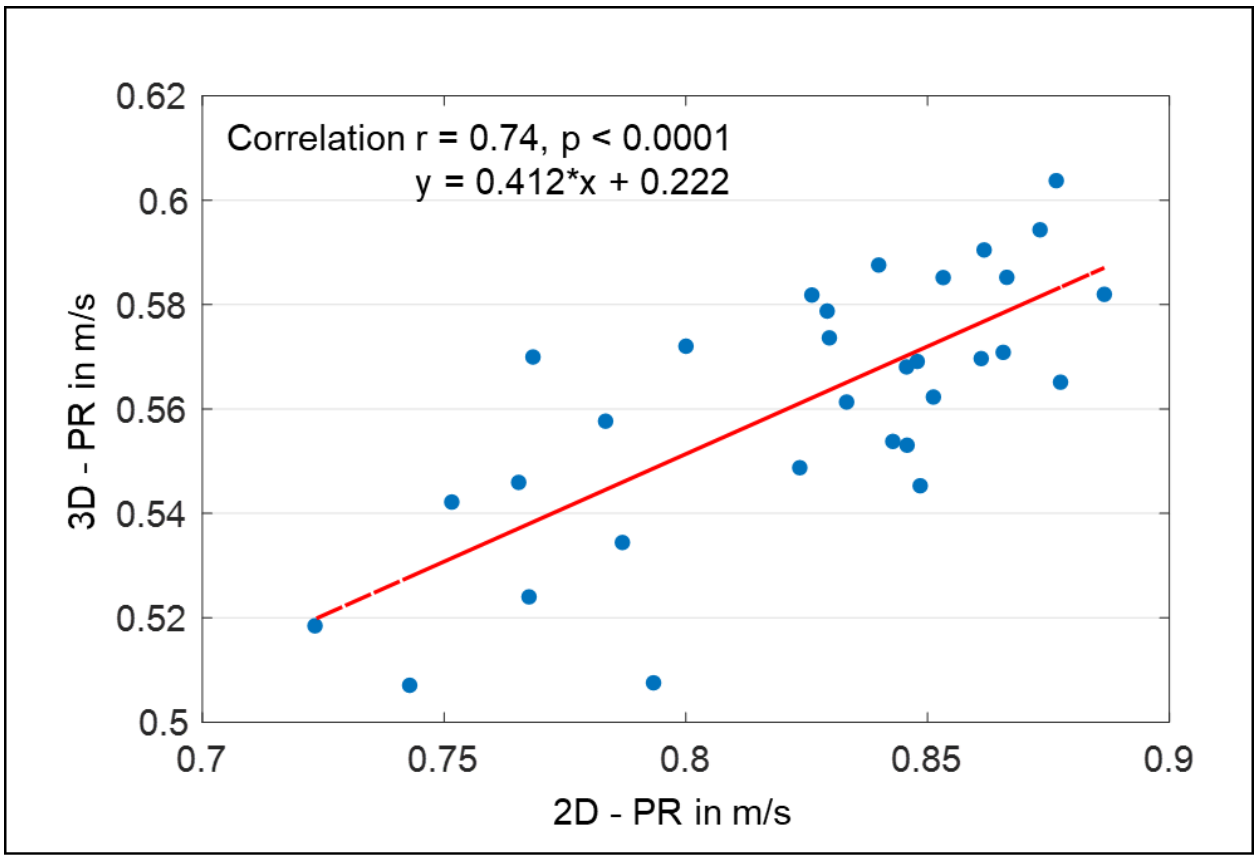

Supplementary Figure 3: Correlation plot for 2D and 3D PR values for global brain tissue.

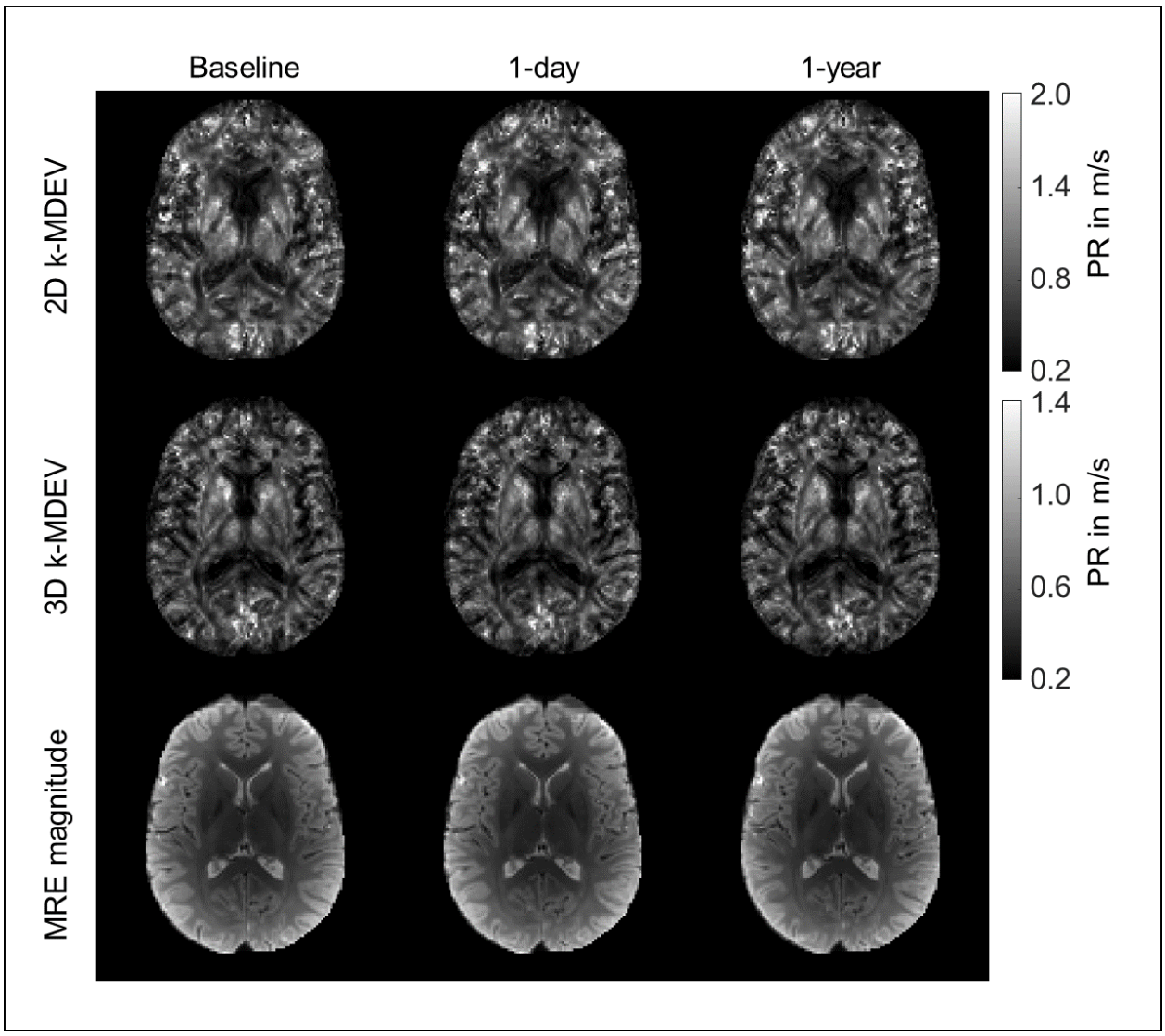

Supplementary Figure 4: Representative MRE penetration rate maps and magnitude images in one subject for three follow-up measurements: baseline, one day later (1-day) and one year later (1-year) for 2D (top) and 3D *k*-MDEV based reconstructions (bottom).

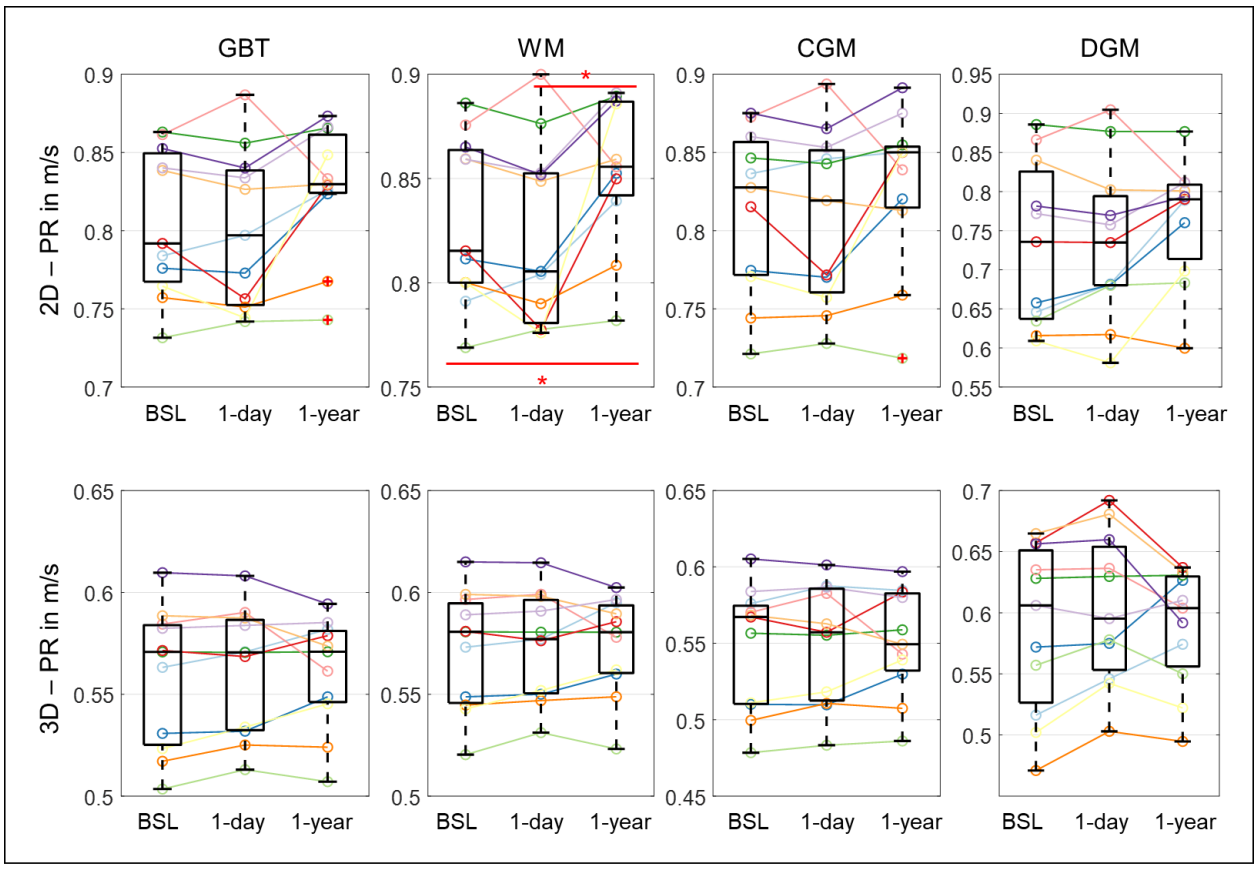

Supplementary Figure 5: Group averaged PR values for 2D (top) and 3D processing (bottom) in global brain tissue (GBT), white matter (WM), cortical gray matter (CGM) and deep gray matter (DGM). Averages were derived from eleven subjects measured at baseline (BSL), one day later (1-day) and after one year (1-year). Significance levels, indicated by asterisks, were determined from paired t-tests with Holm-Bonferroni correction between BSL and 1-year, as well as 1-day and 1-year.

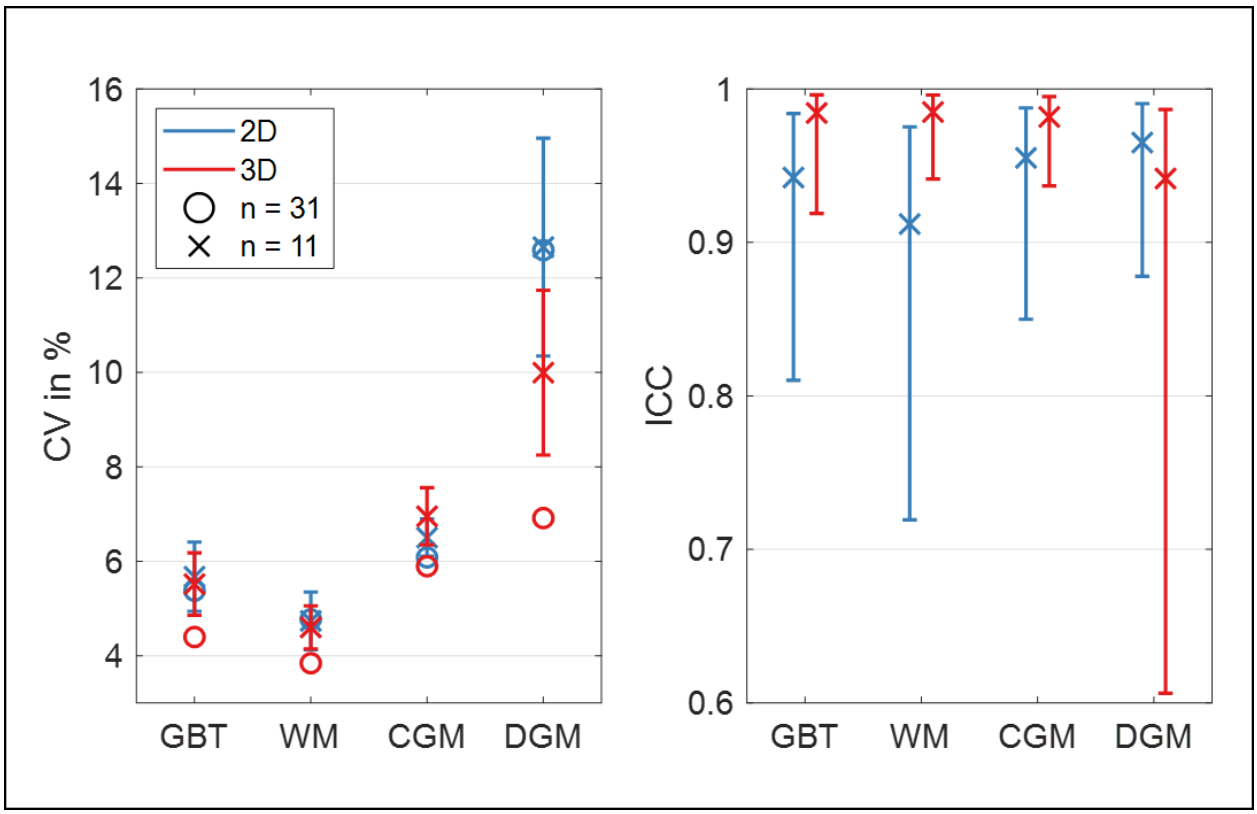

Supplementary Figure 6: Coefficient of variation (CV, left) and intraclass correlation coefficient (ICC, right) for 2D and 3D PR reconstructions for global brain tissue (GBT), white matter (WM), cortical gray matter (CGM) and deep gray matter (DGM). CV determined from single measurement of all subjects and as an average from three CVs for baseline, one day later and after one year repeated tests in eleven subjects. ICC was determined from baseline and after one day repeated measurements.

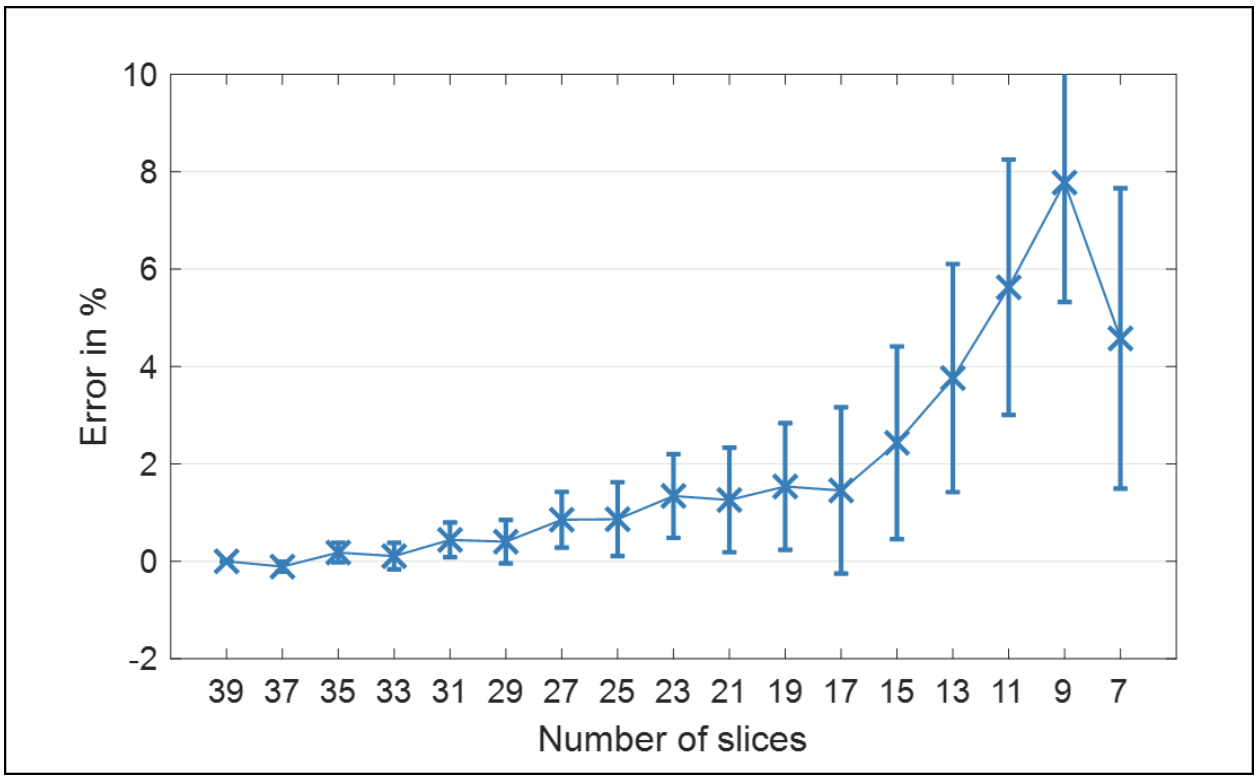

Supplementary Figure 7: Mean relative error in % for eleven subjects for mean white matter PR using 3D data processing. The error is determined by the relative difference between the reconstructed SWS of the center slice using 39 input slices (reference) and subsequently removing the boundary slices prior to the reconstruction.

Tables

Supplementary Table 1: Group mean values for PR for 2D and 3D data processing and the coefficient of variation (CV) for all analyzed brain regions obtained in 31 brains (cross-sectional study): Global brain tissue (GBT), white matter (WM), cortical gray matter (CGM), deep gray matter (DGM), nucleus accumbens (Ac), nucleus caudate (Ca), globus pallidus (Pal), putamen (Pu) and thalamus (Th). Standard deviations are given in brackets. In addition, region size is given.

	2D-PR in m/s	CV in %	3D-PR in m/s	CV in %	Size in cm^3
GBT	0.83 (0.04)	5.4	0.56 (0.03)	4.4	909 (44)

WM	0.85 (0.04)	4.8	0.58 (0.02)	3.8	544 (21)
CGM	0.82 (0.05)	6.1	0.55 (0.03)	5.9	379 (22)
DGM	0.77 (0.1)	12.6	0.6 (0.04)	6.9	53 (5)
Ac	0.7 (0.13)	18	0.68 (0.09)	13.8	1.6 (0.4)
Ca	0.62 (0.13)	20.7	0.57 (0.09)	16.2	10.1 (0.1)
Pal	0.68 (0.11)	16	0.55 (0.07)	12.8	5.5 (0.8)
Pu	0.9 (0.09)	9.5	0.68 (0.05)	7.2	16.5 (1.7)
Th	0.69 (0.12)	17.9	0.5 (0.04)	8.5	26.3 (2.0)

Supplementary Table 2: Coefficient of variation (CV) and intraclass correlation coefficient (ICC) for 2D and 3D PR reconstructions for global brain tissue (GBT), white matter (WM), cortical gray matter (CGM) and deep gray matter (DGM) and DGM subregions. CV is given as an average from three CVs for baseline, 1-day and 1-year measurements for eleven subjects (n = 11). ICC and mean relative absolute difference (RAD) were determined from baseline and 1-day repetition measurements.

2D SWS	mean CV (SD), n = 11	ICC (95%-CI: low, up)	mean RAD (SD, max) in %
GBT	5.67 (0.73)	0.94 (0.81, 0.98)	1.72 (1.22, 4.57)
WM	4.74 (0.61)	0.91 (0.72, 0.98)	1.82 (1.22, 4.74)
CGM	6.50 (0.40)	0.96 (0.85, 0.99)	1.44 (1.48, 5.50)
DGM	12.65 (2.31)	0.97 (0.88, 0.99)	3.11 (2.29, 6.95)
Ac	14.57 (2.57)	0.89 (0.64, 0.97)	4.73 (4.73, 4.92)
Ca	24.96 (4.01)	0.98 (0.92, 0.99)	4.93 (4.93, 2.9)
Pal	16.45 (2.99)	0.94 (0.78, 0.98)	5.49 (5.49, 3.35)
Pu	9.96 (2.2)	0.92 (0.72, 0.98)	4.13 (4.13, 1.87)

Th	17.52 (1.24)	0.98 (0.93, 0.99)	3.16 (3.16, 3.05)
3D SWS	mean CV (SD), n = 11	ICC (95%-CI: low, up)	mean RAD (SD, max) in %
GBT	5.51 (0.66)	0.98 (0.92, 1.00)	0.84 (0.74, 2.00)
WM	4.60 (0.46)	0.99 (0.94, 1.00)	0.62 (0.66, 2.06)
CGM	6.95 (0.61)	0.98 (0.94, 1.00)	1.18 (0.76, 2.20)
DGM	9.99 (1.74)	0.94 (0.61, 0.99)	3.12 (2.78, 7.70)
Ac	13.27 (0.92)	0.82 (0.27, 0.95)	6.71 (6.71, 4.41)
Ca	19.91 (1.96)	0.97 (0.91, 0.99)	3.86 (3.86, 2.86)
Pal	16.43 (1.11)	0.94 (0.78, 0.98)	4.93 (4.93, 4.28)
Pu	10.35 (1.21)	0.92 (0.7, 0.98)	3.53 (3.53, 3.18)
Th	9.29 (2.44)	0.94 (0.4, 0.99)	2.93 (2.93, 2.52)